

# Chapter 2

## Electro-Thermal-Mechanical Modeling of Gas Sensor Hotplates



**Raffaele Coppeta, Ayoub Lahlalia, Darjan Kozic, René Hammer, Johann Riedler, Gregor Toschkoff, Anderson Singulani, Zeeshan Ali, Martin Sagmeister, Sara Carniello, Siegfried Selberherr, and Lado Filipovic**

### 2.1 Introduction

#### 2.1.1 Historical Overview

Before the application of semiconducting materials and the discovery of gas sensors, canaries were taken into mines as an alarm for the presence of harmful gases, such as methane, carbon dioxide, and carbon monoxide. A canary is considered to be a songful bird, but it stops singing when exposed to these types of gases, signaling to the miners to exit the mine immediately.

By the middle of the previous century, it was demonstrated for the first time that certain semiconducting materials show changing conductivity when exposed to some gas molecules, especially when heated to an elevated temperature [1]. Electrical properties of these materials change when the chemical composition of its ambient gas changes. In the early 1960s, Seyama proposed a gas-sensing device based on a thin ZnO film [2]. With a simple electronic circuit, along with a thin film-sensitive layer operating at 485°C, it was demonstrated that the detection of a variety of gases such as propane, benzene, and hydrogen was possible. In 1967, Shaver described a new method to improve the sensing properties of some semiconducting metal oxide (SMO) materials towards reducing gases by an addition of small amounts of noble metals, namely, platinum, rhodium, iridium, gold, and

---

R. Coppeta (✉) · G. Toschkoff · A. Singulani · Z. Ali · M. Sagmeister · S. Carniello  
ams AG, Premstaetten, Austria  
e-mail: [raffaele.coppeta@ams.com](mailto:raffaele.coppeta@ams.com)

A. Lahlalia · S. Selberherr · L. Filipovic  
Institute for Microelectronics, TU Wien, Vienna, Austria

D. Kozic · R. Hammer · J. Riedler  
Materials Center Leoben Forschung GmbH, Leoben, Austria

palladium [3]. Since then, research has intensified for the development of new sensitive materials and micro-hotplates have been designed and optimized with the aim to commercialize the new generation of the SMO gas sensors.

In July 1970, Taguchi filed a patent application in the United States for the first SMO gas sensor device dedicated to safety monitoring [4]. A porous SnO<sub>2</sub>-sensitive thick film was used for this first-generation due to its promising sensing performance. To further enhance its sensitivity, palladium was added to the sensitive layer as a metal catalyst. Afterwards, the sensor was commercialized by Figaro Inc. in alarms for the detection of flammable gases to prevent fires in domestic residences.

Over the last five decades, due to the small footprint, low cost, high sensitivity, and fast response time of the SMO gas sensor, the device has been applied in a variety of applications and in different fields, including food and air quality monitoring, healthcare, electronic nose, agriculture, and so on [5, 6]. The SMO sensor is able to be integrated into a simple electronic circuit, making the potential application of this technology so widespread that specific needs have arisen, which must be satisfied at an industrial level.

Recently, the desire for SMO gas sensors suitable for portable devices such as smartphones and smartwatches has notably increased. New scaling challenges must be overcome in order to enable the practical integration into wearable devices. Low power consumption, high selectivity, and high device reliability are the most common issues considered during gas sensor development. A massive research and development effort is under way to fulfil all the requirements for a good gas sensor performance. The research activities are divided into two main topics: the electro-thermal-mechanical performance of the micro-hotplates and the sensing capability of the sensitive SMO films. This chapter deals with the electro-thermal-mechanical performance and modeling of SMO sensors.

## **2.1.2 MEMS Gas Sensor**

### **2.1.2.1 Definitions**

Micro-Electro-Mechanical Systems (MEMS) refers to technologies used to fabricate miniaturized integrated devices, which combine mechanical and electro-mechanical elements. They are fabricated using micro-fabrication techniques, such as thermal oxidation, photolithography, and chemical vapor deposition (CVD). The physical size of MEMS devices can range from the nanometer to the millimeter scale. These types of devices are used as actuators, controllers, and even sensors in the micrometer range, thereby generating effects on the macroscale. It should however be noted that MEMS devices do not always include mechanical elements; for instance, the SMO gas sensors are fabricated using bulk micromachining, which is a process used to produce micromachinery or MEMS, but have no moving parts. The SMO gas sensor is included in the MEMS fabrication family with the aim to

reduce the power consumption without using mechanical elements. By forming a static membrane as a last step during sensor fabrication, the heat losses from the heated area to the substrate are dramatically reduced.

MEMS gas sensors are broadly based on metal oxides such as  $\text{ZnSnO}_4$ ,  $\text{Nb}_2\text{O}_5$ ,  $\text{In}_2\text{O}_3$ , ITO, and CdO. Among these materials  $\text{SnO}_2$ ,  $\text{WO}_3$ , and ZnO are the most commonly used in the commercial market since they fulfil all the requirements for a good gas-sensing performance at reasonable fabrication costs [7, 8]. The films are deposited on top of suspended micro-hotplates using a variety of techniques and in different forms, namely: thick film, nanobelt, nanotubes, nanowires, thin film, and nanocompound. The operating principle of the MEMS gas sensor relies on heating the sensitive material to high temperatures between  $250^\circ\text{C}$  and  $550^\circ\text{C}$  using Joule heating of an integrated microheater. The working temperature required depends on the sensitive material used and the target gas species. To enable the adsorption and electron exchange between the chemical composition of the ambient gas and the sensitive material, the device must operate at elevated temperatures in the presence of oxygen [9].

### 2.1.2.2 Significance

The market size of gas sensors for consumer applications is expected to reach USD 1297 million by 2023, with a 6.83% compound annual growth rate (CAGR) between 2017 and 2023 [10]. This sector is about to experience the highest growth rate of the sensor market. The main factors responsible for the growth of this business are increasing pollution regulations laid down by governments in developed countries, which mandate the use of gas sensors in potentially hazardous environments, increasing the use of MEMS-based sensor worldwide, and raising awareness of air quality control among users. In May 2018, the World Health Organization (WHO) reported that around seven million people die each year, one in eight of total global deaths, as a result of exposure to air pollution [11]. New data reveal that 90% of the world's population is exposed to fine particles in polluted air, leading to cardiovascular diseases and lung diseases, including heart disease, stroke, lung cancer, respiratory infections, and chronic obstructive pulmonary diseases. Note that, ambient air pollution has caused around 4.2 million deaths, whereas household air pollution has caused about 3.8 million deaths in 2017 alone [11].

Today, wearable devices contain a variety of micro-sensors, such as a light sensor, a pressure sensor, a proximity sensor, an inertial sensor, a hall sensor, and many more. It is very likely that gas sensors will be the next sensor to be integrated in portable devices [12]. Consumer applications are forcing the new generation of gas sensors to minimize size, power consumption, and cost, especially with the use of MEMS technologies. Making gas sensors available to everyone through integration with handheld devices, such as smartphones and wrist watches, allows to monitor air quality easily at any time and from anywhere, thus leading to further increasing awareness about the impacts of climate change. Monitoring indoor and outdoor air quality in real time helps improve the health and quality of life of all human beings.

### 2.1.2.3 Applications

The detection of gases at an affordable price, low power consumption, and with a fast response time, is essential in numerous high-technology fields. This is why the MEMS gas sensor is generating phenomenal interest due to its broad application potential in healthcare, military, industry, agriculture, space exploration, cosmetics, and environmental monitoring. Among other requirements for practical gas-sensing devices, high reliability, low operating temperature, and high selectivity and sensitivity are desired.

One of the major problems faced by gas sensors dedicated to practical applications is to estimate the concentration of a target gas in a realistic ambient, meaning improved selectivity towards a target gas. Unfortunately, MEMS gas sensors are characterized by high sensitivity but have a poor selectivity. To overcome this limitation, an array of gas sensors is used to form an artificial olfactory system. The so-called electronic-nose (E-nose) gathers multiple gas sensors in the same device simultaneously. Each sensitive material is heated to a specific and uniform temperature, as the sensitivity of metal oxide to gases relies on the operating temperature. Measured responses of all sensors are treated using non-parametric analyses in order to distinguish between gases, thus enhancing the sensor selectivity.

Nowadays, the MEMS gas sensor can be found in different applications across the market. Some of the most significant application fields of this sensor are mentioned below.

- Automotive applications: SMO gas sensors can be used to control motor functioning and to help reduce the emissions of harmful gases coming from combustion engines [13]. Indeed, a special packaging must be conceived for these sensors in order to not be influenced by high temperatures in the exhausts.
- Environmental applications: Due to their outstanding features compared to other sensors available in the market, the MEMS gas sensor can also be used to measure and monitor trace amounts of volatile organic compounds (VOCs) in the air [14]. In this area, it is necessary to develop a simple and low-priced device able to monitor indoor and outdoor air quality.
- Medical applications: MEMS gas sensors can be used for clinical diagnostics. The detection of target gases coming from biochemical processes, taking place in the human body, leads to the rapid diagnosis of several diseases [15]. The analyses can be carried out either directly from the patient's skin or from their breath.
- Agricultural applications: To detect rotting fruits and vegetables during storage, MEMS gas sensor can be employed [16].

### **2.1.3 FEM Simulations of MEMS Gas Sensors**

The Finite Element Method (FEM) is a numerical tool which allows solving a continuum physics problem by discretizing the space into a set of subdomains. For example, the geometrical structure of the MEMS sensor is discretized by finite elements in the shape of tetrahedra or hexahedra elements in the 3D case. In this procedure, the field variables like electrical, thermal, or displacement field are approximated by a set of basic functions, for which frequently Lagrange polynomials are used. The mostly used order of polynomial or synonymously order of element is linear or quadratic, which allow linear or quadratic behavior of the field variable within the element. The set of resulting element equations is assembled into a global system of equations and is solved together with the given initial and boundary conditions. From the results of the field variables, relevant parameters like the thermal response time, temperature uniformity, heat losses, and mechanical stresses can be obtained.

The most well-known commercial FEM software tools in the market are Comsol Multiphysics, ANSYS, CoventorWare, MEMS+, and IntelliSense. These tools can be used to apply models which predict how the sensors react to real-world forces, heat, fluid flow, and other physical effects. Before fabrication, MEMS devices are often designed, simulated, and optimized using these Technology Computer Aided Design (TCAD) tools, leading to a reduction in the manufacturing costs and a reduction of the prototype development cycle. TCAD tools contribute significantly in the development of novel and optimized MEMS devices with higher yields. Regarding MEMS gas sensors, these software tools are primarily used to study the mechanical stability of the membrane, the temperature uniformity over the active area, and the power consumption of the sensor.

#### **2.1.3.1 Temperature Distribution**

The appropriate choice of the heater and membrane design are essential to achieve a uniform temperature over the active area, where the sensitive material is deposited. Materials with high thermal conductivities, together with an optimized heater geometry, are usually adopted to achieve the desired temperature distribution. However, using high thermal conducting films increases thermal leakage from the heated area to the Si substrate, thus leading to an increase in the overall power consumption of the device, which is a crucial requirement if the sensors should be integrated with embedded and portable systems. In addition, improving the heater geometry layout with the help of FEM simulations may be difficult in some cases due to the stringent mesh requirements for complex geometrical designs. One practical solution is presented in a recent publication from Lahlalia et al. describing how to efficiently enhance the temperature distribution [17].

The authors in [17] managed to improve the temperature uniformity over the active area without increasing the power consumption of the device. This was achieved by using a novel design, the so-called dual-hotplate, which is based on a single circular microheater along with two passive micro-hotplates. The operating principle of this novel structure depends on the high thermal conductivity of the microheater material compared to the membrane materials. It should be noted that a uniform temperature over the active region is a crucial part for baseline stability since a small change in the temperature over the sensitive material leads to baseline drift, which impacts the accuracy of the gas sensor measurement [18]. To further decrease the heat losses to the substrate, and thereby reduce the power consumption down to a few mW, a new membrane shape is implemented in the dual-hotplate sensor. Curved micro-bridges are used instead of simple beams to enlarge the distance between the active region and the substrate, while preserving the same membrane size.

### 2.1.3.2 Thermal Transient Response

The thermal transient response refers to the time consumed to heat up the microheater from room temperature  $T_c$  to the target temperature  $T_h$ . It is calculated from a simple expression (2.1), where the actual temperature distribution inside the sensor is neglected, while the overall thermal resistance  $R_{th}$  and the overall thermal capacitance  $C_{th}$  of the micro-hotplate are taken into account. The heat balance between the input power  $P_{in}$ , which corresponds to a steady-state heater temperature  $T_h$  and heat losses, can be described by

$$C_{th} \frac{\partial T(t)}{\partial t} = \frac{T_h - T_c}{R_{th}} + P_{in}. \quad (2.1)$$

This equation is solved using Fourier and Laplace analysis with boundary conditions  $T_{(t=0)} = T_c$  and  $T_{(t=\infty)} = T_h$ . The temperature of the microheater is observed to follow exponential behavior with

$$T(t) = (T_h - T_c) e^{-\frac{t}{\tau}} + T_c, \quad (2.2)$$

where  $\tau = R_{th}C_{th}$  is the thermal time constant. As can be seen from the previous equations the thermal time constant depends linearly on the thermal resistance and heat capacity. However, a micro-hotplate with materials having a small thermal resistance and low thermal mass will give a faster response. A small heater exhibits a faster thermal response thanks to the smaller heat capacity, allowing the microheater to operate at very short pulse times, which reduces the power consumption drastically. Note that reducing the sensor's active area and membrane thickness also improves the thermal response time of the micro-hotplate, as the total heated mass is reduced.

### 2.1.3.3 Thermal Simulation

After the design and meshing of the MEMS gas sensor geometry within a TCAD tool, verification of the thermal performance, including the temperature distribution, thermal response time, temperature gradient, heat losses, and heat exchange between the sensor and its environment, are obtained with the help of a design validation software. Indeed, measuring these parameters without the help of FEM tools may be quite challenging, especially if the temperatures are changing quickly, or need to be measured inside the sensor. This means that TCAD software with FEM analysis is an indispensable tool to engineers interested in the detailed thermal performance of their devices.

To model the entire sensor, each part of the structure is represented by a corresponding mesh. The proper choice of the mesh is essential to obtaining accurate approximations. As mentioned earlier, the mesh is a set of elements for which the temperature versus time is calculated. Within each element the temperature is approximated by an ansatz function. One idea is to derive the equation for the temperature at the nodes, which are the centers of the elements. For this approach, temperature and flow variations within the elements are neglected and the node temperature is regarded as representative of the whole element.

This lower order approximation is of linear convergence order. If the heat flow is balanced by the continuity equation of heat energy, we arrive at the finite volume approach. Another concept is to replace the differential equation within each element using finite differences, which is known as the finite-differences method.

All these approaches require equations to be solved at each node at every temperature, generating a large set of equations, which must be solved. One alternative for the thermal problem is to describe the thermal parameters by their electrical equivalent as shown in Table 2.1. For this lumped thermal network, the equations can be solved analytically. For effortless equation solving, standard circuit analysis tools such as LTSpice can be used.

To simulate the heat transfer in a MEMS gas sensor, three mechanisms must be simultaneously taken into account, namely, conduction, convection, and radiation. Generally, radiation is considered to be negligible for temperatures below 600°C

**Table 2.1** Thermal to electric parameter equivalence

Thermal parameter	Electrical equivalent
Temperature $T$ (K)	Voltage $V$ (V)
Specific heat $C_p$ (J/kg K)	Permittivity $\varepsilon$ (F/m)
Thermal resistivity $\rho_{th}$ (K m/W)	Electric resistivity $\rho_{el}$ ( $\Omega$ m)
Resistance $R_{th}$ (K/W)	Resistance $R$ ( $\Omega = V/A$ )
Heat flow $P$ (W)	Current $I$ (A)
Heat $Q$ ( $J = W$ s)	Charge $W$ ( $C = A$ s)
Thermal conductivity $k$ (W/K m)	Electric conductivity $\sigma$ (S/m)
Capacitance $C_{th}$ (J/K)	Capacitance $C$ (F)

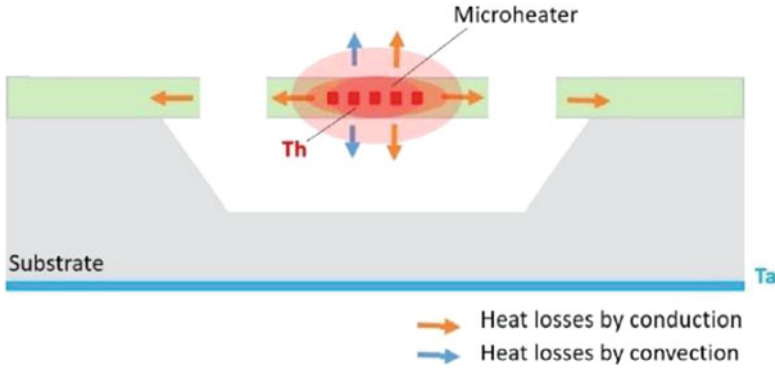


**Fig. 2.1** Heat loss mechanisms through the MEMS gas sensor.  $T_h$  is the temperature of the microheater;  $T_a$  is the ambient temperature

compared to the heat losses by conduction and convection; heat losses in the MEMS gas sensor are caused mainly by heat conduction through the micro-hotplate and the air, and by heat convection, through heat exchange between the external face of the heated membrane and the surrounding air (Fig. 2.1). It must be noted that the amount of heat lost by convection is proportional to the temperature difference between the sensor surface and the surrounding fluid, and to the area of the face exchanging the heat. In addition, natural convection can only occur in the presence of gravity since air movement is dependent on the difference between the specific gravity of cold and hot air. Through this entire discussion, one can deduce that the choice of the membrane and microheater materials and the chosen structure play integral roles in defining the sensor's power consumption.

#### 2.1.3.4 Mechanical Behavior

The design of an effective and reliable MEMS gas sensor is not only a challenge of having a good thermal performance and high sensing capability but also of having an excellent thermo-mechanical stability. To consider mechanical issues during the fabrication stage of the MEMS sensor, one has to analyze the internal stress accumulated in the sensor micro-hotplate. This is one of the major concerns impacting the performance and long-term mechanical reliability of the device. In order to minimize the internal stresses, an appropriate set of process parameters must be found and the fabrication process must be well controlled. Mechanical properties such as density, stoichiometry, orientation, and the average grain size of each layer of the sensor are defined by the specific deposition conditions. In this context, it should be noted that the mechanical characteristics of the sensor layers can be shifted by annealing for one or more cycles. Fortunately, it is possible to adjust these properties by a further annealing step at a specific temperature.

Another problem to be considered during sensor design is the thermal stress. It is introduced on top of the residual stress during operation at high temperature, produced by the difference in the thermal expansion coefficients between membrane materials and by the non-uniform temperature distribution. Thermal stress may lead to a significant increase in membrane deformation and undesirable bimetallic warping effects, which reduces the lifetime of the sensor. Indeed, the operating temperature impacts the mechanical behavior of the sensor, but other thermal effects also play a role. The ultra-short heat pulses influence the mechanical properties since a fast temperature ramp-up may lead to adherence problems or to membrane instability, which may even collapse due to excessive stress changes [19].

## 2.2 Gas Sensor Micro-Hotplate

### 2.2.1 Introduction

The SMO sensor, one of the most widely used sensors for gas detection, requires being heated to an elevated temperature in order to enable a reaction between the sensitive material and a target gas. Therefore, a micro-hotplate, which is a common structure in a MEMS-based gas sensor system, is an essential component for these devices. Additionally, it is required to thermally insulate the active area and the electrical components in order to integrate the sensor with the appropriate analog and digital circuitry.

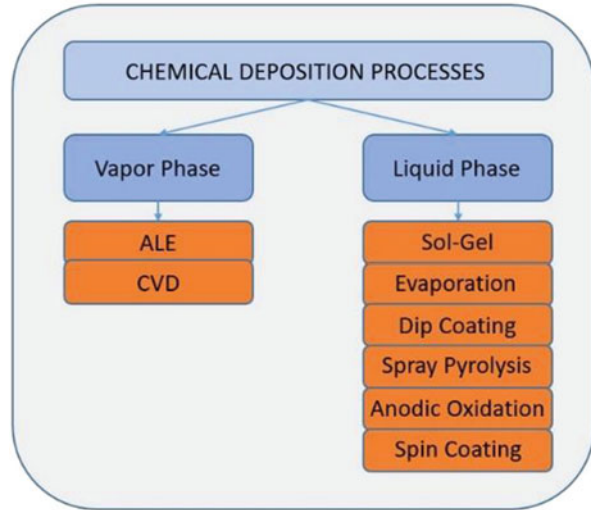
A micro-hotplate is a miniaturized suspended thin membrane which is thermally insulated from the silicon substrate, usually containing a microheater to heat up the sensitive material, a resistive temperature detector (RTD) to estimate the changes in the temperature over the active area, and interdigitated electrodes to measure the electrical resistivity of the sensitive material. Gas sensors based on this type of MEMS structure are very useful for the purpose of minimizing the overall power consumption, enabling the MEMS gas sensor to be applied in the field of chemical micro-sensing. The MEMS-based heating structure can be used for gas-sensing applications after coating its surface with a sensing metal oxide film, which can be deposited, either by liquid phase or by vapor phase deposition, as shown in Fig. 2.2.

### 2.2.2 Microheater

#### 2.2.2.1 Heater Materials and Geometries

The microheater is the key component of the SMO gas sensor, as its primary function is to raise the temperature and maintain a uniform temperature profile over the sensitive material. The area where the sensing layer is deposited is known as the “active region” or “active area.” The level of the operating temperature

**Fig. 2.2** Metal oxide thin film deposition techniques



is dependent on the target gases and the sensitive material used. Therefore, the appropriate choice of the microheater material plays a crucial role in determining the gas sensor's performance and its reliability [20]. The desirable characteristics for a good microheater material are low thermal conductivity, high melting point, high electrical resistivity, low fabrication cost, low thermal expansion coefficient, low Poisson's ratio, and most importantly, high compatibility with MEMS and complementary metal oxide semiconductor (CMOS) fabrication technologies [21].

At the onset of the micro-hotplate development, the commonly used metals for electrical connection in standard integrated circuit (IC) technology such as aluminum and gold were used as a microheater element [22, 23]. Gradually, it was observed that these materials have several drawbacks like oxide formation, low resistivity, poor contact properties, and electromigration effects at high temperatures [21]. In this respect, platinum, which is a very popular heating element for temperature below 500°C, offers better performance such as the ability to deal with high current density, chemical inertness, and high stability of the temperature coefficient of resistance (TCR) up to 650°C [24]. Nevertheless, this material is quite expensive, and its electrical contact formation with other materials is also critical. In addition, platinum has a positive TCR, which magnifies the effect of hotspots, leading to an adverse impact on the long-term reliability of the microheater [21].

Research is currently ongoing to find new materials to overcome the limitations and drawbacks mentioned previously. More recently, nickel and iron-nickel have been used as a microheater, thanks to their low TCR and thermal conductivity [25, 26]. Materials like tungsten [27, 28], nickel-chromium alloys [29], Dilver P1 [30], molybdenum [31], hafnium diboride [32], titanium nitride [33], silicon carbide [34], and Sb-doped SnO<sub>2</sub> [35] have also found to be promising as a heating element owing to the several positive features of these materials, namely, low thermal expansion, resistance to humidity, high Young's modulus, and their non-magnetic

nature. Tungsten was reported by Ali et al. [36] as a good high temperature material for a heater element. Lahlalia et al. [37] presented a Tantalum-Aluminum (TaAl) layer as a resistive microheater on a perforated membrane in silicon nitride. TaAl is characterized by its ability to retain its mechanical strength at high temperature and by its negative TCR of about  $-100$  ppm/ $^{\circ}\text{C}$ , leading to minimal hotspot formation and a stable temperature versus input power curve. The bottom line for choosing a particular heater material is to fulfil the desired requirements; therefore, there are no simple design rules. However, the heater geometry plays a critical and active role to define sensor performance.

Sensitivity, selectivity, and response time are partially dependent on the thermal behavior of the micro-hotplate. Therefore, the proper choice of the microheater design is a crucial factor in determining the sensing performance of the SMO gas sensor. Low power consumption, temperature stability, and temperature uniformity over the sensitive material are three parameters desired while designing the microheater element. To achieve the optimal aforementioned requirements, one simple solution is to alter the microheater geometry. Note that, it is also important to consider the stress induced in the microheater while testing different geometries.

A high stress in the heater element leads to a reduced lifetime of the device. Moreover, current crowding in the corners of the microheater lines is another factor which should be taken into account when choosing the geometry of the heater element. Localized electron accumulation may lead to the generation of microcracks and localized deformations. To overcome this issue, circular type heater structures are reported to be a good alternative to conventional microheater geometries such as the meander shape [38]. Figure 2.3 shows different microheater geometries investigated so far in previous research [39–41].

A new generation of integrated solid-state gas sensors embedded in Silicon on Insulator (SOI) micro-hotplates offer ultra-low power consumption (under 100 mW), high sensitivity, low noise, low unit cost, reproducibility, and reliability through the use of the on-chip integration. The micro-hotplate lies on a SOI membrane and consist of Metal Oxide Semiconductor Field Effect Transistor (MOSFET) heaters which elevate the operating temperature, through self-heating, of a gas-sensitive material. The sensors are fully compatible with SOI CMOS or biCMOS technologies. In addition, the new integrated sensors offer a nearly uniform temperature distribution over the active area at its operating temperature at up to about 300–350 $^{\circ}\text{C}$ . This makes SOI-based gas-sensing devices particularly attractive for use in hand-held battery-operated gas monitors [42].

### 2.2.2.2 Heat Losses

MEMS gas sensor-based micro-hotplate dissipates power through three different mechanisms as already mentioned in Sect. 2.1.3.3.

**Free or natural convection** is the heat transfer occurring between the heated surface of the membrane and the surrounding fluid, including air and other gases. This mechanism is partly described by fluid motion and partly by heat conduction

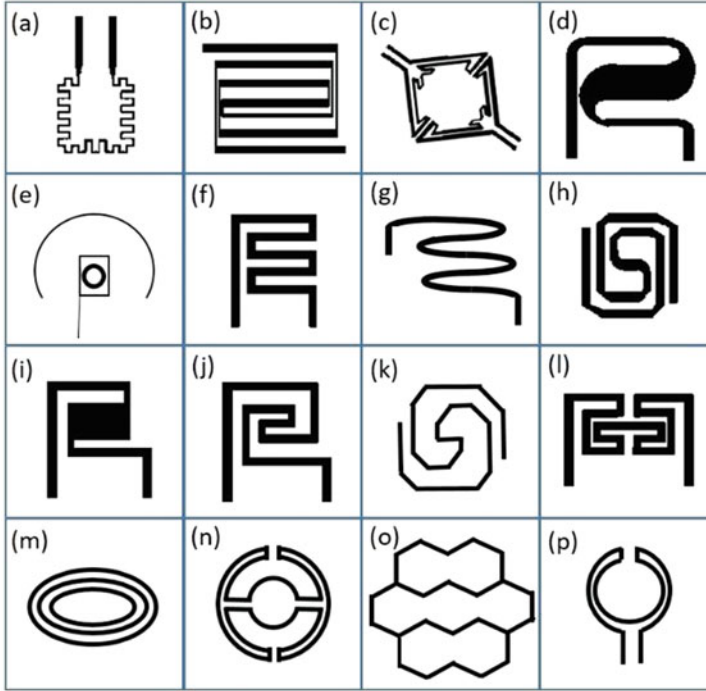


**Fig. 2.3** Different microheater geometries used in MEMS gas sensors. (a) Loop shape. (b) Irregular shape 1. (c) Irregular shape 2. (d) S shape with rounded corner. (e) Plane plate with center square hole. (f) Meander. (g) Curved meander. (h) Curved double spiral. (i) S shape. (j) Double spiral. (k) Double spiral with rounded corner. (l) Fan shape. (m) Elliptical. (n) Drive wheel. (o) Honeycomb. (p) Circular

through the air [43]. Fluid motion can be caused by a gravitational force, as is the case in natural convection, which is the result of temperature differences, or by external energy in the case of forced convection. For convection simulations of the MEMS gas sensor, forced convection is always excluded. Nevertheless, the calculation of the heat losses by natural convection is still very difficult due to the complexity in coupling between the density field, the temperature field, and the fluid field. The total heat flow in natural convection from a heated membrane to the surrounding air can be expressed by Newton's law of cooling as

$$Q_{\text{conv}} = h \cdot A (T_h - T_c), \quad (2.3)$$

where  $h$  is the mean heat transfer coefficient and  $A$  is the exposed area from which the heat flows.

**Heat conduction** must be considered in MEMS gas sensors. This is the heat transfer which occurs between the heated area of the membrane and the substrate. To simplify the model which describes this mechanism, the heat conduction

perpendicular to the membrane is neglected due to the small thickness of the layers which compose the membrane stack. This leads to a one-dimensional heat conduction problem in cuboid coordinates. If the entire suspended membrane is heated to a uniform temperature, the heat conduction occurs only in the suspension beams. For suspended membranes with three suspension beams, heat losses by conduction can be expressed as

$$Q_{\text{cond}} = \frac{3 \cdot \lambda_T \cdot A_{\text{beam}} (T_h - T_c)}{l}. \quad (2.4)$$

Here,  $A_{\text{beam}}$  and  $l$  are the sectional area and length of the beam, respectively, and  $\lambda_T$  is the thermal conductivity of the membrane stack with an  $n$ -multilayer system, which can be calculated by

$$\lambda_T = \sum_{k=1}^n \lambda_k \times t_k / \sum_{k=1}^n t_k, \quad (2.5)$$

where  $t_k$  is the thickness of the layer  $k$ .

**Radiation** is the heat transfer which takes place in the form of electromagnetic waves primarily in the infrared region. Radiation is emitted by a body as a consequence of thermal agitation of its composing molecules. In the MEMS gas sensor, radiation is considered only on the surface of the heated membrane area as the radiation emitted from the interior regions can never reach the surface. Under the assumption that the heated membrane area behaves like a grey body, the heat losses by radiation can be expressed as

$$Q_{\text{rad}} = \epsilon \sigma (T_h^4 - T_c^4), \quad (2.6)$$

where  $\sigma$  is the Stefan–Boltzmann constant, which equals to  $5.67 \times 10^{-8} \text{ W/m}^2\text{K}^4$ . For this type of theoretical model, where the frequency-dependent emissivity is lower than that of a perfect black body, the emissivity  $\epsilon$  must be included. It should be noted that the heat losses through radiation are often neglected since they represent only a few percent of the total heat losses. Nevertheless, due to the  $T^4$  dependency, radiation must be taken into account if the sensor operates at very high temperatures.

### 2.2.3 Membrane Types and Materials

In order to achieve a high temperature with low power consumption, different types of the membranes have been adopted instead of using only Si bulk [21]. A cavity below the membrane of the gas sensor is essential to minimize the vertical heat losses, as the thermal conductivity of the air is much lower than

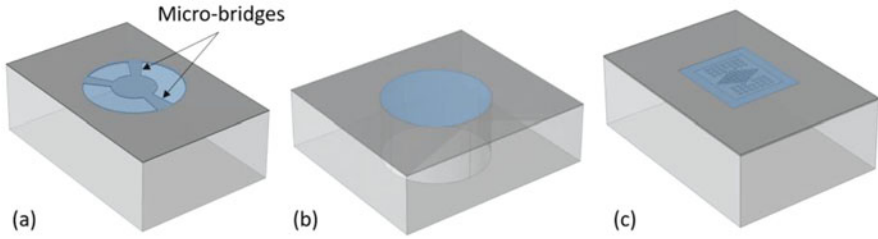


**Fig. 2.4** Schematic of different membrane-type gas sensors. (a) Suspended membrane-type. (b) Closed membrane-type. (c) Perforated membrane-type. The blue color shows where the membrane is formed

the materials used in MEMS and CMOS technology. Up to now, three different structures for the membrane based on SMO gas sensors have been researched, namely, suspended membrane-type gas sensor, closed membrane-type gas sensor, and perforated membrane-type gas sensor. Three-dimensional (3D) views of those structures are depicted in Fig. 2.4.

### 2.2.3.1 Suspended Membrane-Type

The suspended membrane-type gas sensor can be formed by etching the substrate from the front-side using either standard wet etchant with EDP or KOH, or by sacrificial etching [44]. For standard etchant, the sensor surface is first coated with a dielectric layer such as silicon nitride and/or silicon dioxide, then patterned to form the etch windows. The membrane is subsequently released by etching the silicon. In some cases, this step is performed after packaging the sensors with the aim to avoid harsh environments when dicing the wafers, leading to an increase in the fabrication yield. Sacrificial etching is another way to release a suspended membrane, which depends on using the selective formation of porous silicon in a p-type silicon wafer to form a cavity below an implemented n-type silicon layer [44].

One of the primary benefits of using the suspended membrane-type is that it provides low power consumption compared to the closed membrane-type, which is achieved by reducing the thermal mass of the membrane. In addition, this type of membrane is more suitable for CMOS fabrication since there is no need to align the top and bottom sides during the lithography process. Despite these advantages, the suspended membrane gas sensor is less mechanically stable, as the membrane is supported only by micro-bridges. In fact, the residual and thermal stress in the micro-bridge was found to be high and the vertical displacement of the entire membrane was also considerable during operation at high temperature [39].

### 2.2.3.2 Closed Membrane-Type

The closed membrane-type gas sensor can be formed by an anisotropic etching of the silicon from the backside. The etching stops when a solution like KOH or EDP2 contacts the membrane materials. Alternatively, deep reactive ion etching (DRIE), also known as the Bosch process, can be used to etch the wafer backside. DRIE is a multi-cycle process, where each cycle consists of an isotropic deposition followed by an anisotropic etching, usually performed in an ion-enhanced plasma.

This membrane structure is chosen as an alternative to the suspended membrane-type, as the high temperature reached in the beams results in high thermal stress, which may cause the generation of microcracks, leading to a shorter lifetime of the sensor. Recently, novel nanomaterials have been investigated for gas-sensing applications, enabling the detection of gases at low operating temperatures leading to a further exploitation of the closed membrane-type instead of suspended membrane-type to improve the sensor reliability [45].

Usually, the membrane stack of the closed membrane is composed of thin silicon dioxide and silicon nitride layers in order to minimize the intrinsic stress. The silicon dioxide layer has a tensile stress, while the silicon nitride has a compressive stress. For stress compensation, the silicon nitride layer is generally stacked between two silicon dioxide layers. Other materials which have been attempted as a membrane include aluminum oxide [46], polyimide [47], porous silicon [48], silicon oxynitride [49], and silicon carbide [50].

### 2.2.3.3 Perforated Membrane-Type

In order to combine the advantages of both of the aforementioned membrane-types in one structure, the perforated membrane-type was suggested by Lahlalia et al. [37]. This structure is formed by etching the sacrificial layer from the front-side while getting better mechanical performance than a suspended membrane. Moreover, membrane holes which are used for etching the layer below also minimize the lateral heat losses, which reduces the total power consumption compared to a closed membrane-type. The perforated membrane may be classified as a sub-type of the closed membrane since there are no beams supporting the micro-hotplate.

Lahlalia et al. presented for the first time a novel micro-hotplate structure for the SMO gas sensor which includes a pierced TaAl plate as a microheater and a perforated  $\text{Si}_3\text{N}_4$  membrane [37]. To form this membrane structure, polyimide HD8820 is first deposited in a cavity after etching the  $\text{SiO}_2$ , then cured for 1 h at  $350^\circ\text{C}$  to get the desired thickness of  $3\ \mu\text{m}$ . Micro-hotplate materials are deposited thereafter, namely,  $\text{Si}_3\text{N}_4$ , TaAl, AlCu, TiW, and Pt. Finally, the polyimide is etched to release the membrane after opening the holes in the micro-hotplate by highly selective dry etching using a  $\text{CH}_4$ ,  $\text{CHF}_3$ , and Ar plasma.

## **2.2.4 Electrodes and Thermometer**

### **2.2.4.1 Electrodes**

The so-called interdigitated electrodes (IDEs), implemented in the MEMS gas sensor, are used to make the measurements of the gas concentration possible. These electrodes have two functions. On one hand, they measure the resistance change in the sensitive layer, which represents the gas concentration. On the other hand, they act as a catalyst when the electrodes are made by noble materials or their alloys. The catalytic materials promote the interaction between the gas and the sensitive material, leading to an improvement in the sensitivity and response time of the sensor. Usually, when a thick porous-sensing film is used the electrodes are deposited below the sensitive material; however, with a thin film-sensitive layer, they are deposited on top in order to measure the resistance changes on the surface of the sensing layer and to ease the interaction when catalytic electrodes are used. Among the most popular materials used for IDEs are gold [51], platinum [52], AlCu [37], and Al [53]. These materials are often deposited with an adhesion layer, such as a 20 nm of titanium-tungsten, in order to act as a dielectric, to achieve good adhesion, and to prevent delamination [54].

Another aspect which should be considered when using IDEs for MEMS gas sensors is the output signal strength. This is controlled mainly by the design of the active area, and the pitch of the electrode fingers. The proper design and positioning of the electrodes is essential to maximize the gas sensor response towards desired gases. It should be noted that it is very important to maintain a uniform temperature over the IDEs, which must be the same as the microheater temperature for the sensing gases. This can be achieved by forming the microheaters, thermometer, and IDEs in different layers, as the temperature uniformity is better for this combination. Heater and thermometer structures can also be integrated in the same layer with IDEs to ease the fabrication process, but unfortunately, the temperature is less uniform for this configuration compared with the vertical approach [17, 38].

### **2.2.4.2 Thermometers**

Since the operating temperature of the microheater depends on the target gases and the sensitive material, an accurate measurement of the micro-hotplate temperature as a function of the applied power is essential for an optimum performance of the MEMS gas sensor. The extraction of the temperature in these tiny devices is highly challenging due to the extremely small surfaces of the active region. Moreover, this surface is often heated to a non-uniform temperature, which impacts the accuracy of the measurements. Over the past years, different approaches have been adopted for this purpose, including simulations, light glowing, RTD, analytical modeling, and thermoreflectance (TR) [55].

Platinum, a commonly used material for the microheater, has also been used as an RTD since its resistance linearly increases with the temperature [24]. Lahlalia et al. used three types of Pt RTDs instead of one [37], deposited on three different locations over the active region, to additionally characterize the temperature distribution. To further support the obtained results by Pt RTD, the temperature was characterized using CrSi as a temperature sensor. This material has the ability to detect temperatures above 450°C by acting as a phase-change material. Hannef et al. experimentally determined the temperature of the micro-hotplate using TR thermography [27] and proved the accuracy of this method by comparing the obtained results with simulations and silicon RTD.

## 2.3 Material Properties of Micro-Hotplates

### 2.3.1 Introduction

In order to achieve the real-world physical performance of the micro-hotplate in a simulation environment, whether relating to power consumption or mechanical behavior of the membrane, it is essential to use the correct values for the material properties as a function of the operating temperature for all micro-hotplate materials. These material properties can vary due to many factors, such as material thickness, deposition process, and environment conditions. In this section, the main properties, which define the electro-thermal-mechanical performance of the micro-hotplate, are discussed, namely, thermal conductivity, specific heat capacity, Young's modulus, and tensile strength.

### 2.3.2 Thermal Properties

The thermal conductivity and specific heat capacity are the two essential material properties which define the capability of a material to store and transfer heat. Understanding these properties is fundamental for devices which experiences rapid changes in the operating temperature, for any deposition process, or for material which are exposed to large temperature gradients. Precise values for these properties are indispensable for micro-hotplate modeling, for heat management to decrease the power consumption of the device, and for the capability of the device to withstand high temperatures and fast temperature changes in the membrane.

### 2.3.2.1 Thermal Characterization

Thermal characterization of the materials involved in the MEMS gas sensors is crucial for understanding the device behavior and for developing physical models, essential for obtaining predictive simulation results.

For thin layers, mainly electrical resistance thermometry (ERT) or laser-based methods are used [56, 57]. For ERT, an electrically conductive material, acting as a heater, must be placed on top of the layer of interest. If an electrically conductive layer has to be characterized, a thin insulating layer must be placed in between. Alternatively, a p-n junction is used as heater and thermometer. For the named methods, the general principle is the same. Heat is introduced locally into the sample by switching a heat source on and off. The transient temperature curve is determined by the thermal conductivity and the heat capacity.

In the case of ERT, the  $3\omega$  method and the thermal impedance are the dominating methods. The principle of the  $3\omega$  method is that alternating current with frequency  $\omega$  is used for heating, which implies that the power, and therefore also the temperature, shows a  $2\omega$  modulation. Since electrical resistance is a function of temperature,  $3\omega$  frequency components show up in the measured voltage. From the latter, the thermal conductivity can be computed using an analytical model [58]. Recently, this principle was also exploited for scanning probe microscopy, where the scanning thermal microscope (SThM) approaches a nanometer resolution [59]. The thermal impedance method works with the transient temperature response after a step like switching off of the power of a heater [60]. It also allows to characterize a component's thermal response and to calibrate the thermal properties of the materials when an accompanying thermal simulation is performed [61].

In the time-domain thermoreflectance (TDTR) method, a pump laser heats a thin metallic layer ( $\sim 50$  nm) on top of the layer of interest. The reflectance of a probe laser is dependent on the temperature. By using fast lasers, e.g., in the picosecond regime, a very fine resolution in time can be obtained. This allows the measurement of very thin layers down to a thickness of a few tens of nanometers. For example, by varying the pump and probe laser spot diameter, the in-plane, as well as out of plane, thermal conductivity can be measured [62]. This method potentially can also identify the interface conductance and contributions of ballistic transport. This is of utmost importance since as layers become thinner and thinner, the system's behavior can no longer be described using a bulk thermal conductivity alone.

### 2.3.2.2 Thermal Modeling

To calculate the heat flux in the micro-hotplate, the thermal conductivity of materials used must be known, as it provides an indication of the rate at which energy is transferred from the heated area to the substrate. The thermal conductivity depends on the physical structure of matter, which is associated with the state of the matter. From Fourier's law, the thermal conductivity is expressed as

$$\vec{q} = -k\nabla T, \quad (2.7)$$

where  $\vec{q}$  is the local heat flux density in  $\text{W} \cdot \text{m}^{-2}$ ,  $k$  is the thermal conductivity in  $\text{W} \cdot \text{m}^{-1} \cdot \text{K}^{-1}$ , and  $\nabla T$  is the temperature gradient in  $\text{K} \cdot \text{m}^{-1}$ . From the above Eq. (2.7), it is clear that the heat flux increases with increasing thermal conductivity.

The transport of the thermal energy in the materials which compose the micro-hotplate can be attributed to two mechanisms, namely, migration of free electrons and vibrational movements of the atoms/ions. The latter are called phonons in the case of periodic crystalline structures. Even if strictly speaking there are no phonons in solids without periodicity in structure and composition, e.g., in amorphous materials, with the propagons and diffusons, there are the so-called non-localized modes which behave similar to phonons [63]. From kinetic theory, thermal conductivity is defined as [64]

$$k = \frac{1}{3} C \cdot \bar{c} \cdot \lambda_l. \quad (2.8)$$

For conducting materials,  $C$  is equivalent to the electron-specific heat ( $C_e$ ),  $\bar{c}$  is the mean electron velocity, and  $\lambda_l$  is equivalent to the electron mean-free path ( $\lambda_e$ ), whereas in non-conducting materials,  $C$  is equivalent to phonon-specific heat ( $C_{\text{ph}}$ ),  $\bar{c}$  is the average speed of sound, and  $\lambda_l$  is the phonon mean-free path ( $\lambda_{\text{ph}}$ ). Regarding materials where the electrons and phonons carry thermal energy at the same time, thermal conductivity may be expressed as

$$k = k_e + k_{\text{ph}}, \quad (2.9)$$

where  $k_e$  represents the heat transfer in the solid caused by electrons and  $k_{\text{ph}}$  represents the heat transfer in the solid caused by phonons. In alloys, with a high electrical resistance, the interaction between the atoms and the lattices decreases, leading to increased  $k_{\text{ph}}$  in such a way that it becomes no longer negligible compared to  $k_e$ . It should however be pointed out that the regularity of the lattice arrangement has a significant effect on  $k_{\text{ph}}$ . For instance, quartz, which is a crystalline material with well-ordered lattices, exhibits a higher thermal conductivity than amorphous materials like glass.

The calculation of the bulk thermal conductivity is described above for material with relatively large dimensions. However, in many fields of technology like MEMS and CMOS gas sensors, the materials' dimensions can be in the order of few micrometers down to several nanometers. In that case, care must be taken to account for the possible alteration of the thermal conductivity as the dimensions of the sensor layers are smaller.

Figure 2.5 shows the cross section of silicon dioxide with thickness  $t$  along with phonons which contribute to the transport of the thermal energy. When  $t$  is significantly larger than  $\lambda_l$ , as is the case for a bulk material, the effect of the boundaries on thermal conductivity is negligible. However, when the ratio  $t/\lambda_l$  is close to one, as is the case for thin films, boundaries of the film act to scatter the

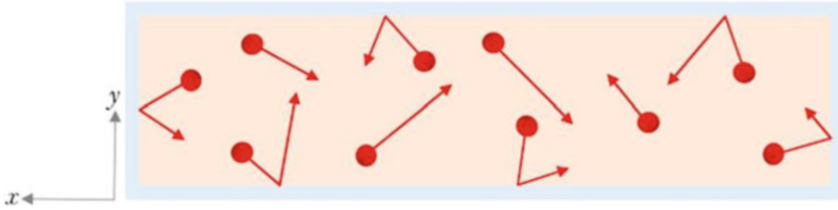


**Fig. 2.5** Phonon trajectories in a silicon dioxide thin film with boundary effects

phonons, which eventually redirect their propagation. As a result, the average net distance traveled by the phonons decreases, which reduces the thermal conductivity of the thin film silicon dioxide. It should be noted that the effect of boundaries on phonons moving in the  $y$ -direction is more significant than phonons moving in the  $x$ -direction. Therefore, for thin films with small  $t/\lambda_l$ ,  $k_y$  is less than  $k_x$ , where  $k_x$  and  $k_y$  are the effective conductivity in parallel and perpendicular to the average flow in the film, respectively.

According to the analysis of Flik and Tien [64],  $k_x$  and  $k_y$  can be obtained as follows:

$$\lambda_x = k (1 - 2\lambda_l / (3\pi t)) \quad (2.10)$$

$$\lambda_y = k (1 - \lambda_l / (3t)) \quad (2.11)$$

The use of the bulk thermal conductivity rather than the effective conductivity results in an error greater than 5% if  $t < 7\lambda_l$  (for  $k_y$ ) and  $t < 4.5\lambda_l$  (for  $k_x$ ). When  $\lambda_l < t < t_c$ , the microscale effect must be taken into account, as  $k_x$  and  $k_y$  are reduced from the bulk value  $k$ . For instance, the critical film thickness  $t_c$  of silicon dioxide in the  $y$ -direction ( $t_{c,y}$ ) and  $x$ -direction ( $t_{c,x}$ ) are 4 nm and 3 nm, respectively, and  $\lambda_l$  is 0.6 nm at 300 K [65]. If  $0.6 \text{ nm} < t < 4 \text{ nm}$ , the effective conductivity should be calculated using (2.10) and (2.11). One must keep in mind that, in a solid,  $\lambda_l$  decreases as the temperature increases, which results in a reduction of the thermal conductivity. Typical values for the thermal conductivity and capacitance of W, SiO<sub>2</sub>, and Si<sub>3</sub>N<sub>4</sub> for different thicknesses and under a variety of temperatures, obtained through a literature study, are provided in the Appendix Tables 2.3 and 2.4 respectively.

### 2.3.3 Mechanical Properties

#### 2.3.3.1 Mechanical Testing

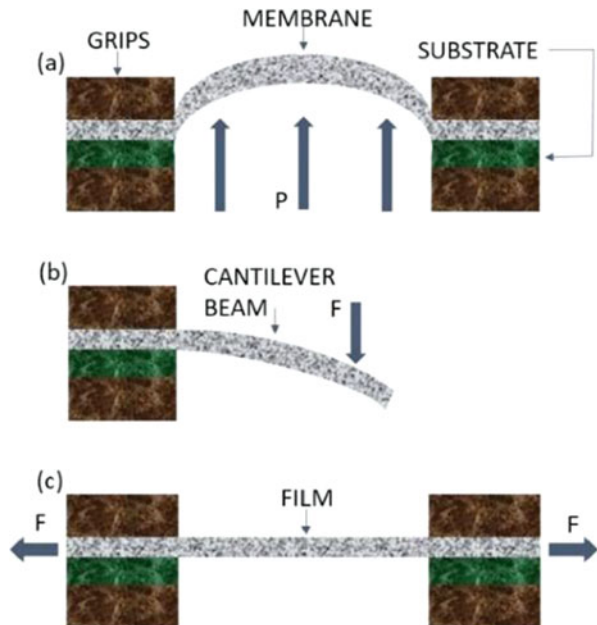
The mechanical properties of semiconductors and metals have become the subject of an extensive research field to understand the mechanical behavior of the gas sensor during operation. The harmful effects that stresses cause in the membrane,

electrodes, thin film-sensitive layer, and the microheater have prompted a plethora of research to determine the origin and the magnitude of stress as well as the means of minimizing stresses. Stress is almost always present in the thin films which constitute the MEMS gas sensor. Note that stress exists even when thin films are not heated or loaded due to the presence of residual stress. The residual stress directly impacts a variety of phenomena, including the generation of crystalline defects, adhesion, and the formation of film surface growths. Another issue which must be addressed is the stress effect in very small regions, which must be measured, understood, and controlled as the gas sensors continue to shrink in size. The build-up of stress and its high concentration in small regions can lead to cracking and delamination, ultimately resulting in failure. The methods to model fracture mechanics and crack evolution are given in Sect. 2.5.2.

A variety of methods have been used in the past with the aim to determine the mechanical properties of thin films, especially their strength [66]. The most common techniques are depicted in Fig. 2.6. Each technique gives values of the Young's modulus ( $E$ ), strength, and internal stress in films. In this subsection, the testing techniques are separately described to evaluate the information gained and compare their advantages.

**Bulge testing** [67, 68] is commonly used to determine the mechanical properties of membrane and thin films in general. This testing method is based on fixing the membrane ends to the ends of a hollow cylindrical tube. To extract the mechanical performance, the membrane is pressurized with gas, then the maximum deflection corresponding to the height of the hemispherical bulge in the membrane is measured

**Fig. 2.6** Methods for mechanical properties testing for thin films. (a) Bulge testing. (b) Microbeam bending. (c) Tensile testing



with an interferometer or a microscope and converted to the strain. The equation which governs the relationship between the height ( $h$ ) and the applied differential pressure ( $P$ ) is given by

$$P = \frac{4th}{r^2} \left[ \sigma_i + \frac{2Eh^2}{3(1-\nu)r^2} \right], \quad (2.12)$$

where  $t$  and  $r$  are the thickness of the membrane and specimen radius, respectively;  $\sigma_i$  is the residual stress in the membrane under a zero pressure differential, and  $\nu$  is the Poisson's ratio.

**Microbeam bending or focused ion beam** [69–74] is used to extract the mechanical properties of the cantilever microbeams, fabricated using micromachining techniques involving photolithography and etching processes. Typical dimensions of the beams are smaller than 1  $\mu\text{m}$  thick, 20  $\mu\text{m}$  wide, and 100  $\mu\text{m}$  long, allowing the cantilever microbeams to be deposited at different locations on the wafer. This allows for a local monitoring of stress variations in subsequently deposited thin films. To determine the Young's modulus and the yield strengths of the thin film materials which comprise the cantilever beam, load–deflection data along with beam theory are used. This data are obtained with the aid of a submicron indentation instrument which continuously monitors the load and deflection caused by a nanoindenter [69].

**Tensile testing** [75, 76] is used to determine how materials will behave under a tension load in order to evaluate both the elastic and plastic response of thin films. In a simple tensile test, a thin film is typically pulled to its breaking point to extract the ultimate tensile strength of the material. The amount of force ( $F$ ) applied to the extremities of the thin film sample and the elongation ( $\Delta L$ ) of the sample are measured during the experiment. Note that the force is applied by electromagnetic force transducers, and the elongations are generally measured by optical methods. In micro-tensile testing, an electron microscope is used to enable a direct observation of the defects during straining. Mechanical properties of materials are often expressed in terms of stress ( $\sigma$ ), which is the force per unit area, and strain ( $\varepsilon$ ), which is the percent change in length. To obtain the stress, the applied force is divided by the thin film's cross-sectional area ( $\sigma = F/A$ ). Strain is measured by dividing the change in length by the initial length of the sample ( $\varepsilon = \Delta L/L$ ). The numerical values of stress and strain can then be presented as a graph called a stress–strain curve.

### 2.3.3.2 Thermal Stress

The thermal effect is another issue which contributes dramatically to the film stress. Films heated to high temperatures and then cooled to room temperature will experience a thermal stress. Films which are cooled from room temperature to cryogenic temperatures or thermally cycled will also be thermally stressed. The magnitude of the thermal stress can be expressed as

$$\sigma = E\alpha (T - T_0), \quad (2.13)$$

where  $\alpha$  is the coefficient of thermal expansion, and  $T - T_0$  is the temperature difference.

For bilayer combinations such as film/substrate, the strain in the film and the substrate are, respectively, expressed by

$$\varepsilon_{\text{film}} = \alpha_{\text{film}}\Delta T + F_{\text{film}}(1 - \nu_{\text{film}}) / (E_{\text{film}}t_{\text{film}}w), \quad (2.14)$$

$$\varepsilon_{\text{sub}} = \alpha_{\text{sub}}\Delta T + F_{\text{film}}(1 - \nu_{\text{sub}}) / (E_{\text{sub}}t_{\text{sub}}w), \quad (2.15)$$

where  $F_{\text{film}}$  is the thermal mismatch force,  $w$  is the width, and  $t$  is the thickness. When the strain of film and substrate are identical  $\varepsilon_{\text{film}} = \varepsilon_{\text{sub}}$ ,  $F_{\text{film}}$  can be obtained by

$$F_{\text{film}} = w (\alpha_{\text{sub}}\alpha_{\text{film}}) \Delta T / \left\{ \frac{1 - \nu_{\text{film}}}{t_{\text{film}}E_{\text{film}}} + \frac{1 - \nu_{\text{sub}}}{t_{\text{sub}}E_{\text{sub}}} \right\}. \quad (2.16)$$

In the case  $\frac{t_{\text{sub}}E_{\text{sub}}}{1} - \nu_{\text{sub}} \gg \frac{t_{\text{film}}E_{\text{film}}}{1} - \nu_{\text{film}}$ , the thermal stress in the film can be expressed as

$$\sigma_{\text{film}}(T) = \frac{F_{\text{film}}}{t_{\text{film}}w} = \frac{(\alpha_{\text{sub}} - \alpha_{\text{film}}) \Delta T E_{\text{film}}}{1 - \nu_{\text{film}}}. \quad (2.17)$$

It should however be noted that the signs are consistent with dimensional changes in the film and substrate. In the case of  $\alpha_{\text{film}} < \alpha_{\text{sub}}$ , thin films prepared at high temperature will be residually compressed when measured at ambient temperature, as the film shrinks less than the substrate.

### 2.3.3.3 Intrinsic Stress

Thin film deposition techniques are widely used for the fabrication of the components of the SMO gas sensors, including microheater, membrane, sensitive layer, insulation layer, and electrodes. During deposition of these thin components, an intrinsic stress  $\sigma_i$  is generated, which, in combination with the unavoidable thermal stress,  $\sigma_{\text{film}}(T)$ , forms the internal or the so-called residual stress ( $\sigma_{\text{film}}$ ). Thus to extract  $\sigma_i$ , the thermal stress given in (2.17) must be subtracted from the measured value of  $\sigma_{\text{film}}$ .

Over the past 40 years, the intrinsic stress has prompted scientists to search for a universal explanation of their origins. According to Dorner and Nix [77], the intrinsic stress observed in thin films comes from the following main sources:

**Grain Growth** Intrinsic stress (compressive stress) in a thin granular film is built up by grain growth, which occurs by normal boundary migration when the initial grain is below the critical value in terms of size [78]. Small islands of depositing film form on the layer below and as they grow, stress builds up at their interfaces.

**Grain Coalescence** During the thin film growth, cohesion starts to occur between the islands as they grow and the gaps between them are small enough, making the participating islands elastically strained, which causes a tensile stress in the thin film [79]. This process creates grain boundaries in the film.

**Annihilation of Excess Vacancies** Intrinsic stress (tensile stress) also builds up due to the gaps caused by vacancy annihilation at grain boundaries and inside grains. A gap in matter causes atoms in the crystals to move towards each other in order to fill this void, leading to a planar contraction in the thin film, if it is not deposited on the substrate. Otherwise, the substrate prevents contraction, which leads to the build-up of tensile stress [77].

**Annealing of the Film** To produce a better crystalline arrangement and an increase the material density, an annealing step is required after the deposition of metals on the substrate [80]. This step results in a shrinkage in the thin film, which eventually leads to build up a tensile stress as the substrate works to prevent the film from shrinking.

**Insertion of Excess Atoms** One of the ways to add atoms to the film during a film growth process is to incorporate excess atoms into the grain boundaries [81]. This mechanism leads to the development of a compressive stress in thin films [82].

**Misfit Stress** Intrinsic stress can be built up during the deposition process as the lattice constant of the thin film is different for the lattice constant of the substrate. The crystal lattice of the thin film and the substrate are forced to line up perfectly at the interface, especially during the initial stage of thin film deposition [83]. Note that the misfit stress can also arise between the grain boundaries since the neighboring grains have different crystal orientations.

## 2.4 Electro-Thermal and Mechanical Simulations

Simulations are performed using FEM to model the thermo-electrical-mechanical behavior of the SMO device during use. The geometry of the calibration device was designed using a commercial Computer Aided Design (CAD) software SolidWorks and imported into the FEM simulation software (COMSOL). One example of a micro-hotplate is shown in Figs. 2.7 and 2.8.

In general, a membrane made of silicon oxide is suspended over a cavity in the silicon substrate. The membrane contains the heater, which is made of tungsten and is connected with two arms to the electrical circuit. In addition to the heater, the membrane contains one heat spreading plate made of tungsten and one layer of silicon nitride, forming the passivation layer of the membrane. The electrodes for gas sensing are deposited above the membrane. Further connections between the heater and the power source can be embedded in the arms. The heater, which is embedded in the membrane, can have various shapes, as discussed in Sect. 2.2.2.1. In general, the heater and the other embedded layers are very thin compared to

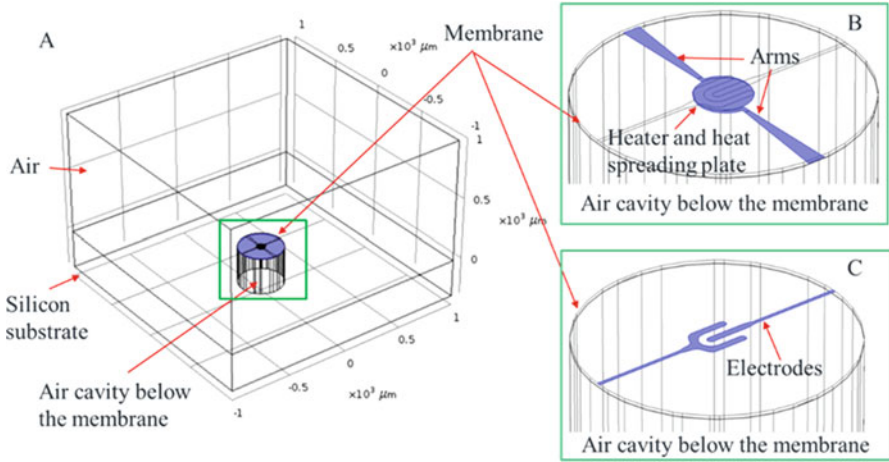


**Fig. 2.7** Simplified geometry of the device used in the FEM model. In inset **A**, the hotplate is surrounded by the silicon substrate and the air. In inset **B**, the heater and the heat spreading plate inside the membrane are shown together with the air cavity below it. In inset **C**, the electrodes above the membrane are shown

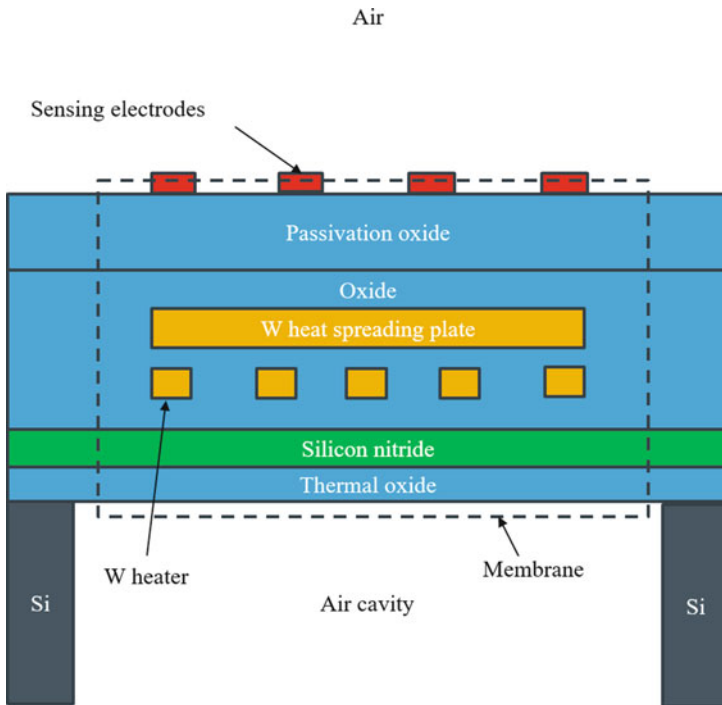


**Fig. 2.8** Schematic of the layers composing the membrane of the hotplate

the full membrane thickness. It should also be noted that all layers are effectively thin films, i.e., the thickness is much smaller than the width and depth, which are defined in the plane of the membrane. When these components are meshed using 3D volume elements, the large aspect ratio of each thin layer causes a poor quality of the mesh elements or an enormous number of elements, which cannot be calculated in a reasonable time, on commercial desktop computers. There are several ways to manage this issue. One way to generate an improved 3D volume mesh is to define an initial two-dimensional (2D) mesh in the plane of the membrane and to sweep it through the direction orthogonal to the membrane plane. This allows to design a 3D mesh which can have a lower number of elements in comparison to direct 3D meshing the volume. This is a very effective method when all layers have equal widths and lengths and are stacked on top of each other; however, it becomes quite difficult and time consuming when the thin layers have different shapes so that the sweeping of the mesh becomes not straightforward. A second solution is drawing the thin layers as bi-dimensional objects and models them using the shell elements feature, as described later in this section. This solution simplifies sensibly the geometry of the structure and saves calculation time and effort, but the conditions to use the shell elements have to be carefully reviewed to avoid non-physical results.

Once the device geometry is finalized, the FEM software requires the definition of the material properties. It is paramount to choose the appropriate material parameters that the FEM model needs. In the case of the micro-hotplate simulation, a literature study of the characteristics of the materials composing the micro-hotplate is necessary, which was performed, and the results are summarized in the tables in the [Appendix](#). Unfortunately, a literature study could not always provide realistic values for all the properties necessary to perform the simulations, as the published values can vary significantly. The reason is that some properties, such as the thermal conductivity, can significantly depend on the fabrication process, which can influence the quality of the crystal structure of the layers. In particular, the deposition temperature, the growth speed, and all other factors which determine the distribution and size of the crystal grains are critical [84]. In addition, the thickness of the layers can change the material properties, as we show in the [Appendix](#). One of the key thickness-dependent parameters is the stress developed in the layer during its deposition. This is called intrinsic stress and it strongly depends on the thickness of the layer. The intrinsic stress of thin layers influences the deformation and the eventuality of fracture of the structure, but it is very difficult to find realistic values of the material properties valid for the desired conditions and designs in literature. Therefore, it is best to calculate them using wafer bending measurements [84] or to use the methods described in Sect. 2.3.3.1 for mechanical properties testing of thin films.

A sensitivity analysis of the input parameters is suggested to understand which of them have the highest influence on the results. Based on our experience, important parameters for the electro-thermal behavior of the device are the electrical conductivity of the heater and the thermal conductivity of the materials composing the membrane. In addition to those, eventual metallic paths connecting the heater,

or the heater area, to the chip can remove more heat from the active area, thereby increasing the power consumption; therefore, the properties of the metallic paths become of increased importance.

When the device is biased, its temperature is increased by a value dependent on the applied bias. Many material properties, such as the electrical and thermal conductivity, but also the Young's modulus, can vary with the temperature, as discussed in Sect. 2.3 and shown in the Appendix. Most FEM tools allow for the implementation of the dependence of the material properties on the temperature. This allows for more realistic results, at the cost of increased simulation time.

Once the geometry and the material properties of the device are defined, it is necessary to model the physics of the problem. When the device is biased, an electrical current runs through the circuit, reaching the heater. This is a resistive element and some power is dissipated due to Joule heating. The material and the shape of the heater are chosen in order to provide the desired amount of power dissipation while improving the heat distribution at the desired location, as discussed in more detail in Sect. 2.2.2.1. The Joule heating causes an increase in the temperature, heating the sensitive material, which can interact with the gas molecules. The increasing temperature also has a collateral effect. The material forming the membrane and the sensing layer has different coefficients of thermal expansion (CTEs). This causes mechanical deformation when the device is biased and could lead to fracture if the design is not optimized to take this into consideration.

All these considerations lead to the need to model both the electro-thermal and the thermo-mechanical behavior of the device. The procedure is described in the following. At first, the electrical component is modeled as an AC/DC circuit, depending on the bias applied. Then Joule heating is calculated and transferred to the thermal model, as defined by the heat equation. The Joule heat is the energy source term which has to be included in the heat equation. Subsequently, the heat equation is solved and the temperature distribution is transferred to the mechanical model of the simulation. In particular, the temperature increase is used to calculate the deformation caused by the difference of the CTEs. This forces the membrane to bend with respect to the original position. Finally, Hooke's law relates this deformation to the stress distribution inside the device. The possibility of fracture caused by the stress and the methods to limit it are discussed in Sect. 2.5.2.

The first step to model the electrical behavior is to set the terminals which define the difference in potential across the circuit. Based on our experience, it is not necessary to draw and model the entire electric circuit but only the part embedded into the membrane. In relation to Fig. 2.7, this is the heater with the two arms, depicted in inset B. Subsequently, the extremities are set as the terminals of the circuit, where the bias is applied. The circuit can be modeled using simple three dimensional elements if the thickness of the heater has comparable dimensions with the width and the depth. If not, the meshing operations could be difficult and produce elements with a poor quality. Consequently, it is necessary to refine the mesh by increasing the number of elements, which increases the simulation time. To overcome this issue, it is faster to draw each thin layer as a shell element defining its thickness in the shell interface. This may reduce the accuracy of the simulation,

but only minimally, considering that the normal component plays almost no role in a thin film's behavior. When a DC bias is applied, the electric behavior is described by

$$\nabla \cdot \vec{j} = Q_{j,v}, \quad (2.18)$$

$$\vec{j} = \sigma \vec{E}, \quad (2.19)$$

and

$$\vec{E} = -\nabla V, \quad (2.20)$$

where  $\vec{j}$  is the current density,  $Q_{j,v}$  is the current source,  $\sigma$  is the electrical conductivity,  $\vec{E}$  is the electric field, and  $V$  is the applied potential. When the shell element is used, the equations are modified to use the tangential gradient operator, which removes the normal component from the gradient operation, so that only tangential components remain. This is mathematically expressed for the potential field  $V$  as

$$\nabla_{\vec{T}} V = \nabla V - (\nabla V \cdot \vec{n}) \cdot \vec{n}. \quad (2.21)$$

Thus, the normal gradient operator is

$$\nabla_{\vec{N}} V = (\nabla V \cdot \vec{n}) \cdot \vec{n}. \quad (2.22)$$

In case a shell element is used, the equations are modified as

$$\nabla_{\vec{T}} \cdot (d_s \vec{j}) = d_s Q_{j,v} \quad (2.23)$$

and

$$\vec{E} = -\nabla_{\vec{T}} V, \quad (2.24)$$

where the subscript  $s$  denotes the layer and  $d_s$  is the thickness of the layer.

After the electrical behavior is modeled, it is necessary to describe the thermal problem using the heat equation, which is defined over the entire structure in the stationary case as

$$\nabla \cdot (k \nabla T) = -Q_j, \quad (2.25)$$

where

$$Q_j = \vec{j} \cdot \vec{E}. \quad (2.26)$$

Here,  $T$  is the temperature,  $k$  is the thermal conductivity,  $Q_j$  is the Joule heat, and the heat flux is represented by

$$\vec{q} = -k\nabla T. \quad (2.27)$$

The layers, which are much thinner compared to the total thickness of the membrane, can be drawn and modeled as bi-dimensional elements. The boundary conditions of these thin layers require the definition of their real thickness. If a thin layer is a bad thermal conductor compared to adjacent elements, the tangential heat flux can be neglected and only the heat flux across the layer's thickness is considered. When the thin layer is instead a good thermal conductor, the temperature difference and the heat flux across the layer's thickness are neglected and only the tangential flux is considered. In our simulations, the general case, where both the tangential and normal heat fluxes are considered in the calculation, is assumed:

$$\nabla_{\vec{T}} \cdot \vec{q}_s = Q_s \quad (2.28)$$

$$\vec{q}_s = -k_s \left( \nabla_{\vec{T}} T_s + \nabla_{\vec{N}} T_s \right) \quad (2.29)$$

Here,  $Q_s$  is the Joule heat and  $\vec{q}_s$  is the heat flux in the layer.

The heat equation as presented before includes the conduction, but not the convection of the heat, which could take place in the air. In the simulated cases, the convection has a negligible impact on the results; therefore, it is not included in the FEM model. A deeper discussion on the sources of heat loss is given in Sect. 2.2.2.2.

Once the mathematical equations describing the electro-thermal behavior of the device are defined, it is necessary to choose appropriate boundary conditions (BCs) to ensure realistic results. Appropriate BCs have to be assigned also to the physical boundaries of the FEM model. In fact, it is not possible to include the entire electronic circuit around the sensor in the FEM model as it would require an unmanageable computational cost. Therefore, it is necessary to exclude it and assign appropriate BCs to the extents of the model.

In our simulations, a good match between the FEM results and the experimental data is obtained when the hotplate is surrounded by a thick layer of silicon. The reason is that, in reality, the hotplate is connected to the heat source through the arms and is isolated by the silicon from other metallic paths. Therefore, there are no other metal interconnections which could cause heat losses to the system.

The external surfaces of the silicon domain are assumed to be thermal insulators, i.e., the heat flux through them is zero. Our simulations show that this condition ensures realistic results of the FEM simulation if the distance between the sensor and the external surfaces of the silicon domain is at least double the membrane diameter of the gas sensor. This implies that the system can dissipate the heat only through the

air. This is a reasonable assumption because the heater is in the central area of the membrane and the membrane is thin and wide. Thus, most of the heat is dissipated through the interface between the membrane and the air. A small amount of heat is transferred to the silicon surrounding the membrane; however, this is insignificant compared to the dissipation through the air. If the external surfaces of the silicon domain are far enough from the membrane, the heat is again dissipated through the interface between the silicon and the air. In addition, the FEM simulations show that at such conditions, no relevant heat flow is present in the silicon substrate far from the membrane; therefore, it is assumed that no thermal leak happens through the silicon substrate. The system with such boundary conditions could represent in reality a membrane realized on a silicon die, which is embedded inside an insulating material. However, if the membrane is close to a metal line connected to an external circuit, the metal line would be an additional path for the heat to dissipate. In such situations, the metal line has to be considered in the simulation, together with different boundary conditions for the external surfaces of the system.

Above the sensor, air is represented by a one-millimeter-thick domain (Figs. 2.7 and 2.8). The temperature of the external boundary of the air domain is constant at room temperature. With such boundary conditions, our FEM simulations show that a thinner air domain influences the temperature and power dissipation of the hotplate, making the results unrealistic. Hence, it is necessary to keep the external border of the air domain far enough from the hotplate. In addition, in the FEM model the cavity below the membrane is filled with air, and the temperature of the bottom surface of the air cavity is constant at room temperature as well.

The meshed FEM model of the structure in Fig. 2.7 is composed of 290,250 elements and it was solved in about 30 min using the previously described mathematical equations and relevant BCs. The hotplate is subjected to a different bias and the resistance and the dissipated power of the conductive layers, i.e., the heater and the arms, are calculated and compared with the measured data. Figures 2.9 and 2.10 show a good match between the FEM results and the experimental data of both the resistance and the dissipated power, respectively. The resistance is measured at every applied bias. The experimental value of the dissipated power is calculated by multiplying the measured electrical current with the measured resistance. Figure 2.11 shows the comparison between the temperature of the hotplate and the one obtained from the experimental data. In particular, the latter is calculated based on the following formula

$$R = R_{25} \left( 1 + \alpha (T - 25) + \beta (T - 25)^2 \right), \quad (2.30)$$

where  $R$  is the measured resistance for a specific bias,  $R_{25}$  is the measured resistance at  $25^\circ\text{C}$ ,  $T$  is the temperature expressed in  $^\circ\text{C}$ .  $\alpha$  and  $\beta$  are empirical parameters, which are determined through an additional experiment. A probe, made of the same metal as the hotplate heater, is located on a chuck. The chuck is heated to different temperatures. Subsequently, the measured values of the resistance and the

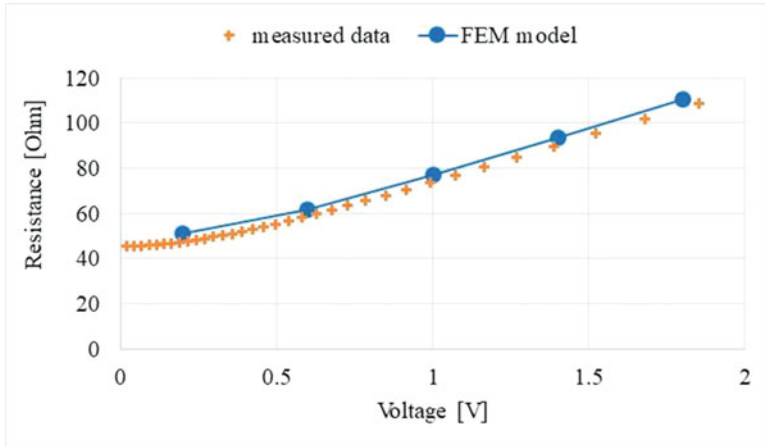


**Fig. 2.9** The resistance of the conductive layer of the sensor is measured and simulated for different applied biases

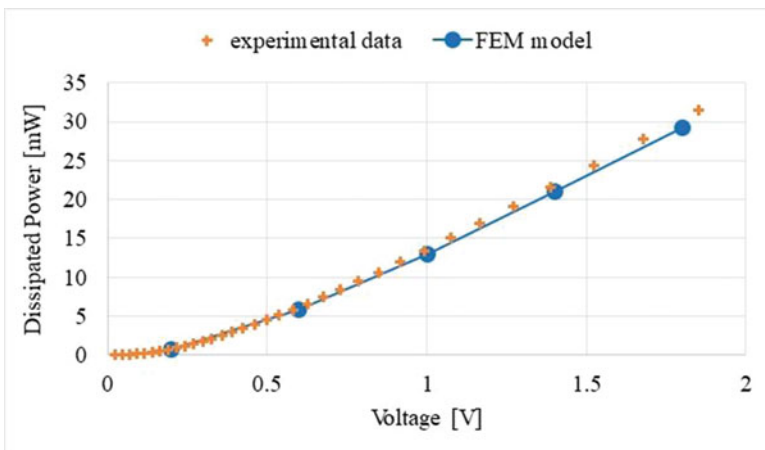


**Fig. 2.10** The power dissipated by the sensor is measured and simulated for different applied biases

temperature define a curve, which is fitted with the previous curve, from which the parameter values for  $\alpha$  and  $\beta$  are extrapolated.

The difference between the temperature profiles obtained from the FEM model and from the experiments at high bias, shown in Fig. 2.11, is most likely caused by the approximated method to define the parameters  $\alpha$  and  $\beta$ .

The FEM model can also accurately reproduce the temperature distribution around the sensor, as shown in the cross section in Fig. 2.12. The clear gradient of the temperature in the air around the sensor suggests that the air takes an active

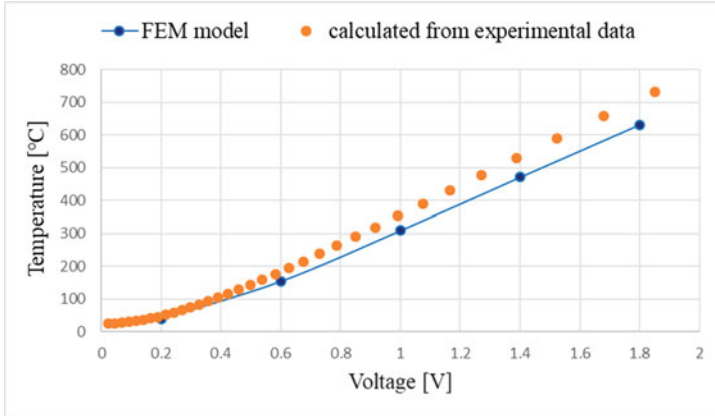


Fig. 2.11 The temperature obtained from the FEM model is compared with the one calculated using the measured resistance

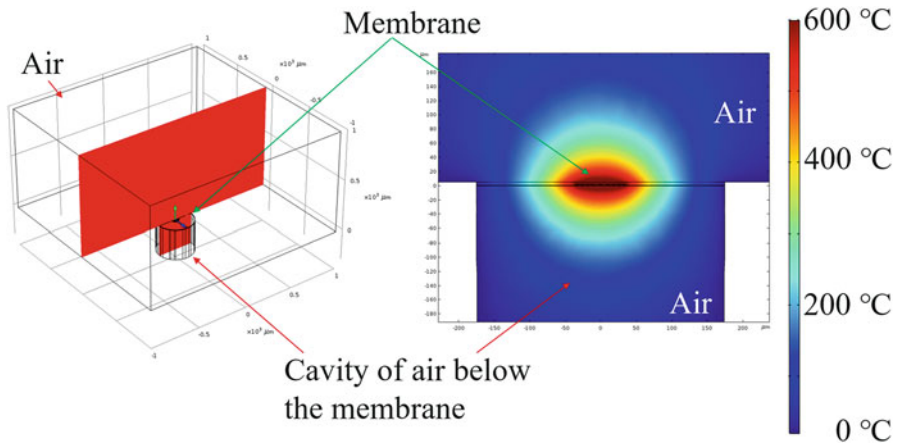


Fig. 2.12 Cross section temperature distribution

role in heat conduction. It is known, from literature, that the thermal conductivity of the dry air increases with temperature [85]. However, if the humidity is taken into consideration, the thermal conductivity decreases at high temperatures. In reality, the physical dynamic of the air around the hotplate is more complicated than pure dry air or humid air. In reality, there would be a dynamic of vapor being created and annihilated by convection and conduction while colder humid air replaces it. Close to the hotplate of the sensor, the dry air is a good approximation of the real conditions because the temperature gradient is really small. Instead, for regions far from the hotplate, this dynamic would not be negligible because the heat conduction

worsens as humid air comes close to the sensor. Therefore, the influence of the humidity on the temperature around the hotplate was simulated.

In our simulations, the relative humidity of the air surrounding the hotplate was varied from 0.25 to 0.75 and the variation of the thermal conductivity of the air was calculated. Figures 2.13 and 2.14 show the thermal conductivity and the temperature, respectively, at a distance of 75  $\mu\text{m}$  away from the heater. In particular, their variation with the applied bias and the relative humidity of the air is evaluated. The results show that a variation of about 15% in the thermal conductivity of air causes a variation in temperature by approximately 5°C, leading us to consider the influence of the humidity on the temperature distribution of the air as insignificant and almost negligible. In reality, it could be the case that the velocity of the air and vapor around the hotplate would increase the impact of the humidity.

The mechanical behavior of the device under operating conditions is critical because the long use, coupled with the high temperatures, can potentially lead to high levels of deformation, such as a bending of the membrane and, in the worst case, to cracking and eventual device failure. The membrane is the most critical area of the device because of its bending during device operation. The bending is related to the stress accumulated inside it. In particular, the membrane is a multilayered structure, as depicted in Fig. 2.8, whose layers deform differently during heating because they have different coefficients of thermal expansion. This type of stress is often called thermal stress, but it is not the only component causing the deformation. As previously described in section 2.3.3.3, the intrinsic stress is an additional type of stress, which develops during the deposition of one layer over a substrate.

The estimation of the intrinsic stress in a layer is based on the measurement of the bending of a substrate, in general a silicon wafer, above which the layer is deposited [84]. However, the intrinsic stress, obtained with such a method, can

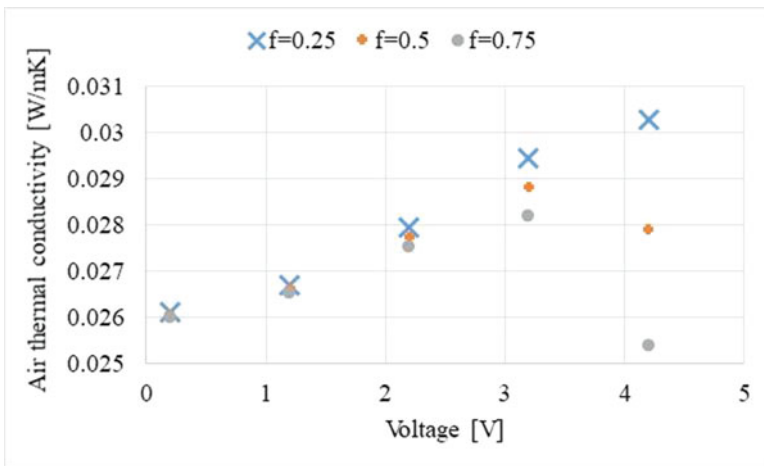


**Fig. 2.13** The thermal conductivity of the air as a function of the applied bias for different values of the relative humidity  $f$  of the air surrounding the device

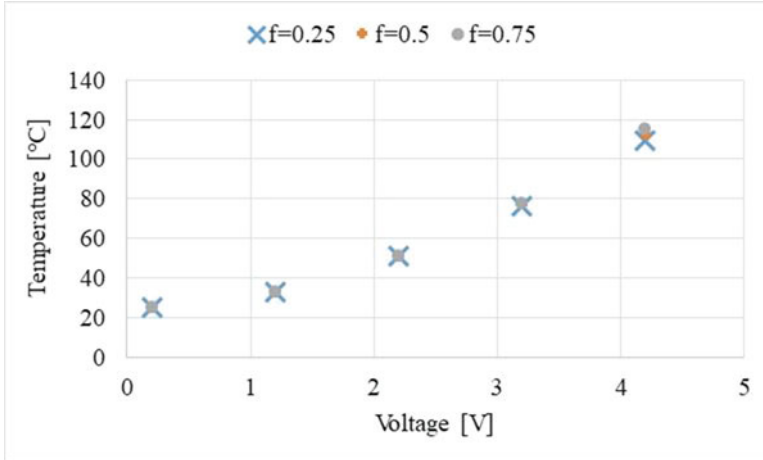


**Fig. 2.14** The temperature of the air as a function of the applied bias for different values of the relative humidity  $f$  of the air surrounding the device

differ significantly from the one in a layer with a different and complex shape and embedded inside an insulating material; this is the case for the heater embedded in silicon oxide (Figs. 2.7 and 2.8). In such conditions, the measurement of the intrinsic stress is difficult and, in order to ensure accurate simulations, it is necessary to calibrate its value in the FEM model with the measured out-of-plane displacement of the unbiased hotplate membrane. The calibration procedure is quite straightforward when the geometry of the structure is simple, but it could become cumbersome and near-impossible when the interfaces among the layers are many and have complex shapes. The intrinsic stresses are added to the FEM model as a boundary condition.

The out-of-plane displacement of a hotplate membrane, similar to the one depicted in Fig. 2.7, along the diameter of the membrane top surface at room temperature was measured with a profilometer prior to applying any bias. The measured profile showed that the membrane bends downward by  $\sim 100$  nm. Simulations of the mechanical behavior of the membrane prior to any bias being applied were performed using measured values of the intrinsic stress for the silicon oxide 280 MPa, the silicon nitride  $-260$  MPa, and for the tungsten 1330 MPa. These values are obtained by measuring wafer bending above which a thin layer of tungsten, oxide, or silicon nitride was deposited [85]. The results of the FEM model prior to any bias (Fig. 2.15) provide a membrane bending with the same order of magnitude of the measured profile. Eventual discrepancies could be caused by the fact that there is some variation in the real intrinsic stresses, which could be different from the calibrated ones used in the simulation.

Once the calibration is complete, the operating conditions are simulated by applying a bias to the device. The stress and the deformation of the membrane are subsequently calculated with the following hypothesis: All materials composing the structure are assumed to behave linearly elastic. Eventual plastic deformation or

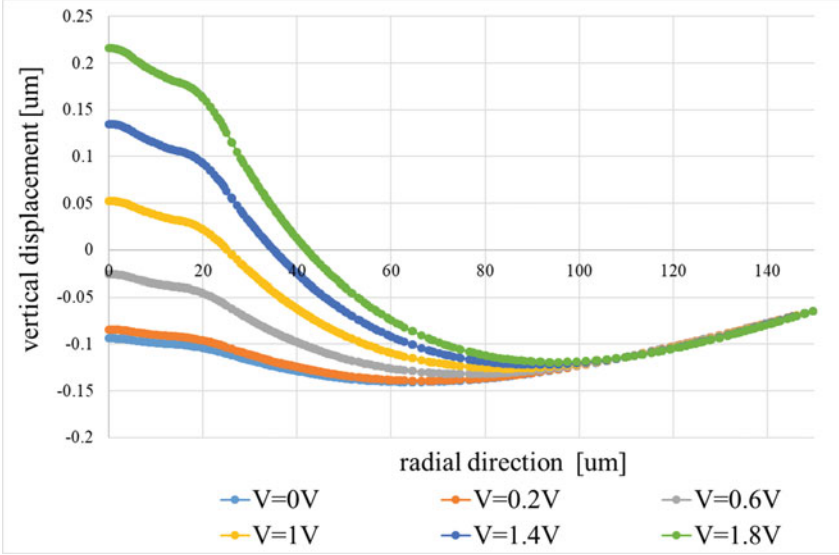


**Fig. 2.15** FEM model results of the out-of-plane displacement of the top surface of the membrane along its radius of the membrane. The hotplate is biased and the deformation is caused by the intrinsic and the thermal stress caused by the temperature increase due to the Joule effect. Zero displacement indicates the un-deformed state of the hotplate

creep phenomena of the heater and the other metallic layers inside the membrane are negligible when they are made of tungsten. In fact, we performed some experiments of temperature-driven stress relaxation of polycrystalline tungsten films, deposited on a silicon wafer, close to the tungsten deposition temperature. The results show that the creep and the consequent stress relaxation are negligible in the first 5 h of experimental observation. Afterwards, these two phenomena are no longer negligible. When the heater of the micro-hotplate is made of polycrystalline silicon, no plastic deformation or creep behavior are expected with normal operating conditions. Therefore, in our devices, both creep and plasticity are neglected on the basis of the experimental observations and the linear elasticity theory is used in the FEM model, as described below.

The Joule heating causes the deformation of the structure because it is composed of materials having different coefficients of thermal expansions. In particular the elastic strain of a layer, with the CTE  $\alpha$ , caused by heating  $\Delta T$  is

$$\varepsilon_{th} = \alpha \cdot \Delta T \quad (2.31)$$

Assuming that the materials behave linearly elastic, they are described by Hooke's law, which relates the elastic strain  $\varepsilon_{el}$  and the stress  $S$  as

$$S = S_0 + C : \varepsilon_{th}, \quad (2.32)$$

where  $C$  is the stiffness tensor, which depends on the Young's modulus and the Poisson ratio only in the case of an isotropic body and  $S_0$  is the intrinsic stress of the layer. In a notation where the indices are shown, the same equation would read

$$\sigma_{ij} = S_{0,ij} + \sum_{k=1}^3 \sum_{l=1}^3 c_{ijkl} \varepsilon_{kl}. \quad (2.33)$$

The displacements are calculated as

$$\varepsilon_{th} = \frac{1}{2} \left[ (\nabla \vec{u})^T + \nabla \vec{u} \right], \quad (2.34)$$

where  $\vec{u}$  is the displacement vector. In case the thin layers are modeled using shell elements, the equation is slightly modified as

$$\varepsilon_{th} = \frac{1}{2} (\nabla_t \vec{u}). \quad (2.35)$$

One boundary condition of the mechanical model is that the bottom surface of the silicon domain (Fig. 2.7) is physically fixed, i.e., the displacements in the three orthogonal directions are zero. In addition, the intrinsic stress of each layer could be neglected, as a result of the calibration. If the device is not directly subjected to any externally applied loads, the intrinsic and thermal stresses are the only stress types considered in the FEM model.

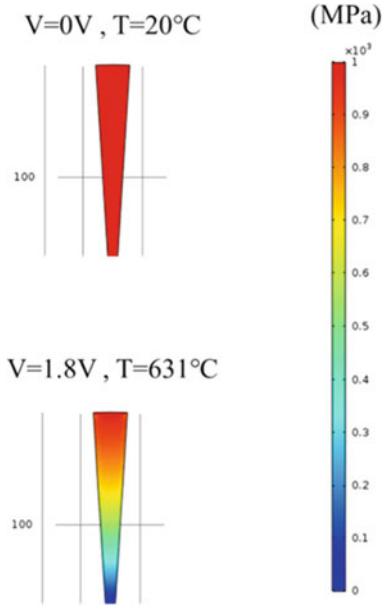
Considering the hotplate membrane shown in Figs. 2.7 and 2.8, thin layers (i.e., the heater, the heat spreading plate, and silicon nitride) are simulated using shell elements in our FEM model. Using the equations of the mechanical behavior, coupled with the electro-thermal model described previously, the simulation provides the profile of the membrane displacement on its out-of-plane direction for different applied biases (see Fig. 2.15).

In general, the membrane bends downward at 0 V as a result of the relaxation of the intrinsic stress. The center of the membrane, which contains the W heater and heat spreading plate, has an upward displacement of about 100 nm.

Increasing the applied bias up to 1.8 V, the displacement of the central area increases from  $-100$  nm to 200 nm as a result of the Joule effect. Since the heating concerns more the central area of the membrane, as it contains the heater, the sections of the membrane far from the center are less displaced.

The results show another interesting effect of Joule heating. At room temperature, i.e., when no bias is applied, the maximum principal stress along the heater and the arms is approximately equal to the intrinsic one, inserted as a boundary condition. Increasing the bias, i.e., the temperature, the stress in the W heater decreases. This happens because the W heater has a higher CTE with respect to the oxide, thus the heater expansion is limited by the oxide and a compressive stress is created and it compensates the initial high tensile stress. The consequence is that the total stress is gradually reduced by increasing the bias, i.e., increasing the temperature.

**Fig. 2.16** FEM model results of the maximum principal stress along the arms of the heater



Despite this, Fig. 2.16 shows that the stress in the arms remains high at high bias, instead of decreasing. This happens because the Joule effect is weaker in the arms than in the heater, thus no compressive stress is created during the heating. During the operating lifetime of the hotplate, the device is continuously switched on and off, but this does not reduce the stress in the arms; therefore, the arms could be subjected to damage deriving from cycling fatigue. These phenomena deserve more experimental investigations in order to be proven and a more sophisticated mechanical model should be developed.

## 2.5 Fracture Modeling for Mechanical Robustness of Sensor Components

Thermo-electrical characterization and modeling of components for microelectronic applications, such as gas sensor hotplates, are very well established in the research activities of the microelectronic industry. With the progress towards new materials and complex designs, the need for mechanical stability of the components is increasing. The reliability of thin film stacks can be improved if the material properties and internal mechanical loading conditions are properly utilized. Initial defects, due to manufacturing, cannot be excluded and for that reason a device should be designed in order to be failure tolerant. The two major questions which have to be addressed are: Is there a fracture parameter that can properly describe crack propagation in such systems and how can we determine the crack driving force in thin film stacks.

### ***2.5.1 Residual Stresses in Thin Films for Gas Sensor Hotplates***

Special attention has to be paid to the role of residual stresses on failure processes and their influence on the reliability and functionality of components [84, 86]. Residual stresses in thin films used in microelectronic components, such as gas sensor hotplates, can reach very high values, i.e., in the order of GPa [87–90]. Even if the average residual stress within the layer or in layer stacks does not seem to be critical, strong stress gradients can appear [89, 90]. The local residual stress values can even exceed the tensile, compressive or shear strength and interface strengths of the materials, leading to cracking and delamination within the component [91]. In general, residual stress is composed of intrinsic stress, formed during deposition, and extrinsic (thermal) stress stemming from the mismatch in the coefficient of thermal expansion between the individual layers and the substrate [84], as discussed in Sect. 2.3.3.

Two groups of methods, which enable local and depth resolved residual stress characterization have evolved over the last years. Within the first group we find X-ray methods performed in grazing incidence or in transmission. Recent development of the latter uses focused synchrotron X-ray beams [92–95]. The second group includes methods where a specific region with characteristic features is imaged before and after local removal of a stressed material using, for example, ion beam milling. The form of the processed area can have numerous geometrical shapes [70, 71]. This results in a local relief of residual stress and a consequential deformation of the sample, from which the strains and stresses can be reconstructed analytically or using finite element modeling, when the stiffness is known [72, 73, 96, 97]. In contrast to the X-ray methods, these methods work without the need for the presence of crystalline phases and can also be applied to amorphous materials.

In many applications, small amounts of residual stresses are tolerable and do not have a significant influence on the performance or reliability of a device. On the other hand, residual stresses have been shown to have decisive impact on the crack driving force in a material when high enough. While tensile residual stresses, in general, increase the crack driving force, compressive residual stresses are desired because of their crack stopping capabilities. In the case of compressive residual stress, however, the risk for delamination increases [84]. Thus, in order to increase the reliability of microelectronic components in general, and gas sensor hotplates in particular, it is of uttermost importance to work on increasing the failure resistance of the components on the one hand (e.g., layer design for fracture toughness, interface strength) and the reduction of failure driving forces (e.g., CTE mismatches and intrinsic residual stress engineering) on the other.

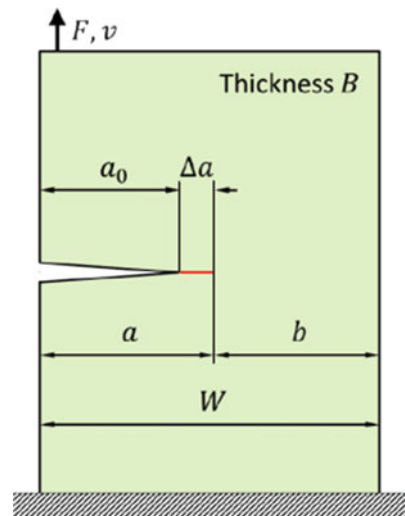
## 2.5.2 Fracture Mechanics for Thin Films in Gas Sensor Hotplates

The topic of fracture mechanics is one of the most active fields of research and was already extensively investigated in the past. The basics of fracture mechanics are collected in different books and publications [98, 99]. The book by Kolednik [100] gives a very good overview of fracture mechanics. In the course of this section, the most relevant concepts and terms of fracture mechanics are introduced, along with how fracture mechanics applies to thin film structures for sensing applications.

### 2.5.2.1 Definition of the Crack Driving Force

Imagine a homogeneous body with an initial crack under loading, as shown in Fig. 2.17. Generally, this crack with an initial length  $a_0$  will extend if the crack driving force (CDF)  $D$  equals or exceeds the crack growth resistance  $R$  [100, 101]. The CDF  $D$  describes a loading parameter deduced from the strain energy and the work from external loading. The crack growth resistance  $R$  will prevent crack propagation. It depends on the fracture toughness of the material, on the crack extension  $\Delta a$  (because of the increasing size of the plastic zone) and on the geometry (because of the constraint effect), shown in Fig. 2.17. If  $D < R$ , the crack will remain stationary. However, if  $D = R$ , the crack will exhibit stable growth, and if  $D > R$ , crack growth becomes unstable.

**Fig. 2.17** A homogeneous body under Mode I loading. The initial crack length is  $a_0$  and the current crack length is denoted by  $a$  and together with the ligament length  $b$  it gives the specimen thickness  $W$



### 2.5.2.2 Regimes of Fracture Mechanics

In a simple distinction, fracture mechanics can be divided into linear elastic fracture mechanics (LEFM) and elastic–plastic or nonlinear fracture mechanics (E–PFM, NLFM) [100]. The concept of LEFM applies if the plastic deformation during crack growth is zero or limited. In this case, the size of the plastic zone  $r_{pl}$  is very small compared to the crack length  $a$  and the ligament length  $b$ ,  $r_{pl} \ll a, b$ , in which case small-scale yielding (ssy) conditions apply, shown in Fig. 2.18a.

E–PFM, on the other hand, is used if the body experiences significant plastic deformation. In a homogeneous body with a long crack, the prevailing conditions are either large-scale yielding (lsy) or general yielding (gy), as shown in Fig. 2.18b. Under the lsy conditions, the onset of plastic deformation is at the back face of the body, while gy applies when the crack tip plastic zone and back face plasticity merge into one plastic zone. In a special case where the crack is very short, as shown in Fig. 2.18c, E–PFM has to be applied, since also a small plastic zone does not comply with the conditions from Fig. 2.18a. In layered composites, such as thin metallic film stacks shown in Fig. 2.18c, the materials deform in a different way and often the lsy condition cannot be defined by the onset of back face plasticity. In this case, lsy applies if the size of the plastic zone  $r_{pl}$  compares to or is higher than the crack length  $a$ .

### 2.5.2.3 Linear Elastic Fracture Mechanics

The stresses close to the crack tip of a linear elastic body are calculated by [102]

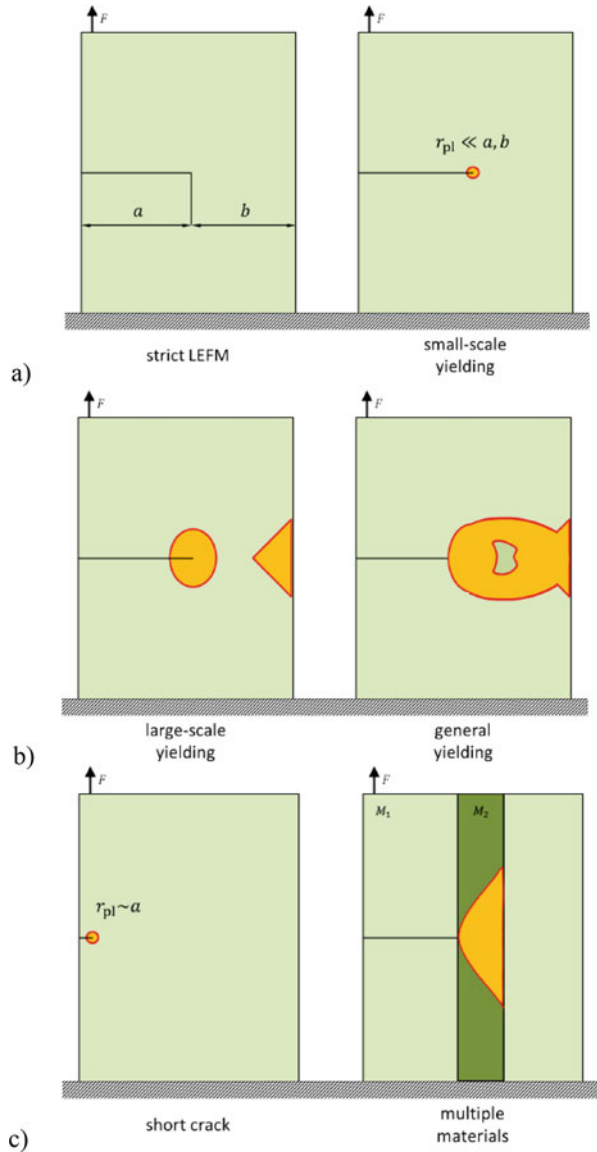
$$\sigma_{ij} = \frac{K}{\sqrt{2\pi r}} f_{ij}(\theta), \quad (2.36)$$

with the polar coordinates  $(r, \theta)$ , the angular stress functions  $f_{ij}(\theta)$  and

$$K = \sigma_{ap} \sqrt{\pi a} f_K. \quad (2.37)$$

$K$  describes the intensity of the near-tip stress field and is therefore called the stress intensity factor. It depends on the applied stress  $\sigma_{ap}$ , the crack length  $a$ , and the geometry of the body, represented by  $f_K$ . However, the equation for the near-tip stresses implies a singular behavior of the stress field, as  $r \rightarrow 0$ , which is not the case in reality. Plastic deformation generated at the crack tip keeps the stresses finite, but for as long as the plastic zone is reasonably small the stress intensity factor  $K$  is a valid measure for the CDF. Moreover, as the stresses or strains at the crack tip equal or exceed a critical value  $K = K_C$ , fracture occurs. The material parameter  $K_C$  is called fracture toughness and describes the resistance of the material against fracture. Connecting this stress and strain deformation concept to the energy-based perspective of a CDF  $D$ , one finds the relation

**Fig. 2.18** Different regimes of fracture mechanics. (a) Linear elastic fracture mechanics. (b) Elastic–plastic fracture mechanics. (c) Special cases of E–PFM and fracture mechanics in composites



$$G = \frac{K^2}{E_b}, \tag{2.38}$$

where  $G$  is the LEFM equivalent to the generalized definition of the CDF  $D$ , called elastic energy release rate [103].  $E_b = E/(1 - \nu^2)$  is the biaxial Young's modulus for plane strain conditions, where  $\nu$  is the Poisson's ratio.

### 2.5.2.4 Nonlinear and Elastic–Plastic Fracture Mechanics

In the regime where plastic deformation becomes relevant, the concept of LEFM will fail. The stress intensity factor  $K$  has to be extended into a parameter valid for NLFM and E–PFM. Based on the deformation theory of plasticity from 1968, a fracture parameter called  $J$ -integral was introduced by Rice [104]. Similar to  $K$ , the  $J$ -integral describes the intensity of the near-tip stress field and crack growth occurs if the corresponding critical value is reached. The  $J$ -integral describes a contour integral on an arbitrary path around the crack tip. It was shown by Rice [99] that the  $J$ -integral is the equivalent to the energy release rate of work done on a nonlinear elastic body containing a crack per unit fracture area. This can be understood as a more generalized version of the elastic energy release rate  $G$ . For LEFM, the  $J$ -integral is identical to  $G$ ; consequently, a relationship between the stress intensity factor  $K$  and the  $J$ -integral can be established:

$$J_{\text{el}} = \frac{K^2}{E_b} \quad (2.39)$$

There are some limitations concerning the conventional  $J$ -integral proposed by Rice when applying it to real elastic–plastic materials, pointed out by Simha et al. [105] and Kolednik et al. [106]. The conventional  $J$ -integral is based on the theory of plastic deformation, assuming nonlinear elastic behavior for elastic–plastic materials. In a real elastic–plastic material, for example, the unloading portion of the stress–strain curve is not following the loading curve, as is the case in NLFM. The material unloads linear elastically, depending on the elastic properties of the material. Thus, the total strain energy density can be split into an elastic and plastic part. The plastic strain energy density is absorbed for plastic deformation in front of the crack tip and the elastic part of the total strain energy density is available to drive crack extension. For a proper description for elastic–plastic materials incremental theory of plasticity is necessary. In this case, the NLFM  $J$ -integral does not directly describe a CDF for real elastic–plastic materials. It acts as a measure of the intensity of the crack tip stress field, comparable to the stress intensity factor  $K$  in LEFM.

Gas sensor hotplates, for example, are constantly subjected to nonproportional loading conditions in operation. Additionally, several inhomogeneities have a distinct influence on the failure behavior in the thin film systems, and render the determination of critical fracture parameters and critical loading conditions difficult.

### 2.5.2.5 Configurational Force Concept and the $J$ -Integral

Material imperfections, smooth or discontinuous material variations, as well as residual stresses, are known to have an influence on the CDF in a body [106–114]. A very convenient way to describe the impact of material inhomogeneities on the fracture behavior is provided by the configurational force concept, which is based on the ideas of Eshelby [115], and adopted by Gurtin [116] and Maugin [117].

This concept makes it theoretically possible to describe any kind of inhomogeneous behavior in a body. Examples for inhomogeneities or imperfections in a material are cracks, voids, dislocations, and sharp interfaces.

In the following, the basic idea of the configurational force concept is given. For comprehensive derivations of the following equations and definitions, the reader is referred to [106, 108, 115–117].

From a thermodynamical point of view, a configurational force (CF) tries to push a defect into a configuration where the total potential energy of the system has its minimum. In general, a CF vector  $\mathbf{f}$  can be calculated at each material point in a body. It is defined as the divergence of the configurational stress tensor  $\mathbf{C}$  and becomes non-zero only at positions of a defect in the body

$$\mathbf{f} = -\nabla \cdot \mathbf{C} = -\nabla \cdot (\phi \mathbf{I} - \mathbf{F}^T \mathbf{S}), \quad (2.40)$$

where  $\phi$  is the Helmholtz-free energy or strain energy density,  $\mathbf{I}$  represents the identity tensor, and  $\mathbf{F}^T$  and  $\mathbf{S}$  are the transposed deformation gradient and the first Piola–Kirchhoff stress tensor, respectively [106, 108].

If, for example, a two-dimensional homogeneous elastic body with a sharp crack is considered, the crack tip exhibits a CF vector  $\mathbf{f}_{\text{tip}}$ , determined by

$$\mathbf{f}_{\text{tip}} = -\lim_{r \rightarrow 0} \int_{\Gamma_r} (\phi \mathbf{I} - \mathbf{F}^T \mathbf{S}) \mathbf{m} dl. \quad (2.41)$$

Here,  $\Gamma_r$  is the contour around the crack tip at the distance  $r$  away from the crack tip and  $\mathbf{m}$  denotes the unit normal vector to the contour. The corresponding energy dissipated per unit crack extension is a projection of  $\mathbf{f}_{\text{tip}}$  in the direction of crack extension  $\mathbf{e}$  and gives

$$J_{\text{tip}} = -\mathbf{e} \cdot \mathbf{f}_{\text{tip}}, \quad (2.42)$$

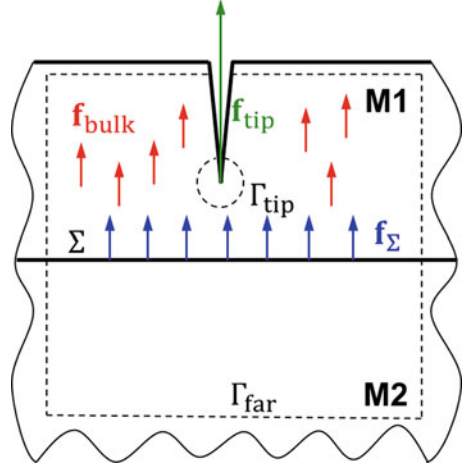
where  $J_{\text{tip}}$  is the scalar near-tip  $J$ -integral and it represents the CDF. If the body is externally loaded the CDF is equal to  $J_{\text{tip}} = J_{\text{far}}$ , where  $J_{\text{far}}$  is the far-field  $J$ -integral, which can be understood as the driving force induced by the external load in the body.

### 2.5.2.6 Material Inhomogeneity Term

Suppose we have a layer stack where two materials M1 and M2, as shown in Fig. 2.19, are separated by a sharp interface (IF)  $\Sigma$ . The material properties, such as the Young's modulus, experience a jump and, therefore, CFs  $\mathbf{f}_{\Sigma}$  are induced at the sharp IF, shown in Fig. 2.19, given by [118]:

$$\mathbf{f}_{\Sigma} = -\left( \llbracket \phi \rrbracket \mathbf{I} - \llbracket \mathbf{F}^T \rrbracket \langle \mathbf{S} \rangle \right) \mathbf{n} \quad (2.43)$$

**Fig. 2.19** An example of a two-material body with a crack. Configurational forces (CFs)  $\mathbf{f}_\Sigma$  at the sharp interface  $\Sigma$  and bulk CFs  $\mathbf{f}_{\text{bulk}}$  inside the material layer **M1** are induced, respectively, because of material property variations. The material layer **M2** does not exhibit bulk CFs, as the material properties are constant



In (2.43),  $\mathbf{n}$  denotes the unit normal vector to the IF. A jump of a quantity at the IF is designated by  $\llbracket q \rrbracket = (q^+ - q^-)$  and  $\langle q \rangle = (q^+ + q^-)/2$  represents the average of  $q$  across the IF, where  $q^+$  and  $q^-$  are the limiting values of  $q$  on each side of the IF.

A continuous variation of material properties can also occur in a body. This circumstance induces additional CFs  $\mathbf{f}_{\text{bulk}}$  inside of the material, as is the case in material **M1** in Fig. 2.19. The bulk CFs are given by the relation [118]

$$\mathbf{f}_{\text{bulk}} = -\nabla_{\mathbf{x}}\phi(\mathbf{F}, \mathbf{x}). \quad (2.44)$$

The strain energy density  $\phi$  in (2.44) depends on the reference coordinate  $\mathbf{x}$  where  $\mathbf{x} = \mathbf{x}(x, y, z)$  and  $\nabla_{\mathbf{x}}$  denotes the explicit gradient in the reference frame. If the material properties exhibit only a variation in the  $y$ -direction, the sole contribution from  $\mathbf{f}_{\text{bulk}}$  is  $\mathbf{f}_{\text{bulk},y}$ .

The CFs induced at the IF  $\mathbf{f}_\Sigma$  and in the bulk  $\mathbf{f}_{\text{bulk}}$  strongly affect the CF at the crack tip and, therefore, the magnitude of the CDF. Two terms can be introduced to quantify those effects [118]:

- **Interface inhomogeneity term**  $C^{\text{IF}}$ , being the sum of all CFs  $\mathbf{f}_\Sigma$  at the IF

$$C^{\text{IF}} = -\mathbf{e} \cdot \int_{\Sigma} \mathbf{f}_\Sigma dl. \quad (2.45)$$

- **Bulk term**  $C^{\text{B}}$ , which is the sum of all CFs  $\mathbf{f}_{\text{bulk}}$  inside of a material layer

$$C^{\text{B}} = -\mathbf{e} \cdot \int_{\text{M}} \mathbf{f}_{\text{bulk}} dA. \quad (2.46)$$

The sum of  $C^{\text{IF}}$  and  $C^{\text{B}}$  results in the material inhomogeneity term  $C_{\text{inh}}$ :

$$C_{\text{inh}} = C^{\text{IF}} + C^{\text{B}} \quad (2.47)$$

The balance of CDFs is therefore fulfilled if the material inhomogeneity term  $C_{\text{inh}}$  is introduced, which renders the CDF to be [108, 118]

$$J_{\text{tip}} = J_{\text{far}} + C_{\text{inh}}, \quad (2.48)$$

where  $J_{\text{far}}$  is calculated around the far-field contour  $\Gamma_{\text{far}}$  as shown in Fig. 2.19. In this context,  $C_{\text{inh}}$  corresponds to the CDF caused by the material inhomogeneities at a given loading  $J_{\text{far}}$  in the body. An anti-shielding effect is described by a positive shielding by a negative value of  $C_{\text{inh}}$ .

In the same way, a material inhomogeneity effect is induced if, instead of the material properties, the eigenstrains or the resulting eigenstresses that exhibit a jump or smooth variation [114, 118].

### 2.5.3 Crack Driving Force in Thin Film Stacks for Micro-Hotplates

In the following, some results for an application of the introduced fracture mechanics concept are presented. The CDF is determined numerically for a tri-layer stack, where a  $0.3 \mu\text{m}$  thin tungsten (W) heater-layer is sandwiched between two  $1.5 \mu\text{m}$  thick silicon dioxide ( $\text{SiO}_2$ ) layers, and positioned on a  $5.0 \mu\text{m}$  thick silicon (Si) substrate, as shown in Fig. 2.20. After performing fracture simulations on a micro-cantilever beam [119], the CDF can be calculated by applying Eqs. (2.43)–(2.48).

Linear elastic and elastic–plastic simulations are performed where tensile residual stresses for  $\text{SiO}_2$  and W are considered as internal loading, denoted by LERS and EPRS, respectively, depicted in Fig. 2.21a.

The material properties used for modeling are given in Table 2.2. Note that after a crack is introduced into the system, the residual stresses have to redistribute in order to reach an equilibrium state, causing a finite CDF value. The influence of the Young's modulus and yield strength inhomogeneity on the CDF is demonstrated for an increasing crack length. For a better understanding, it has to be mentioned that in a homogeneous linear elastic material the CDF, in form of the  $J$ -integral, would increase linearly for an increasing crack length while under the same load. Additionally, the upper and lower dashed lines represent critical  $J$ -integral values  $J_C$  for W and  $\text{SiO}_2$ , respectively, calculated from literature fracture toughness values [120, 121].

As the crack transitions from the compliant  $\text{SiO}_2$  layer to the stiffer W layer, see Table 2.2, the CDF is reduced by the shielding effect from the Young's modulus inhomogeneity at the first IF. When elastic–plastic properties are considered the yield strength inhomogeneity causes a slight increase of  $J_{\text{tip}}$  very close to the first IF compared to the LERS calculation, which was expected as  $\text{SiO}_2$  behaves

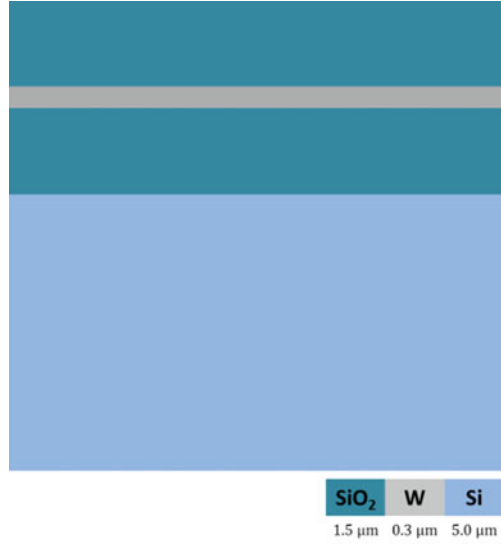


**Fig. 2.20** Example for a thin film stack for numerical determination of the crack driving force

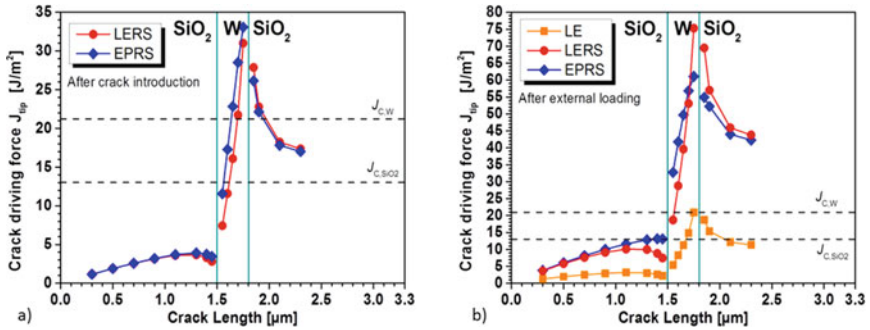


**Fig. 2.21** Crack driving force  $J_{tip}$  variation in the  $\text{SiO}_2/\text{W}/\text{SiO}_2$  thin film stack. The critical  $J$ -integral values for both materials are represented by dashed lines. **(a)** Crack driving force caused by residual stress redistribution after introducing a crack into the system. **(b)** Crack driving force for the different model considerations after external loading is applied

**Table 2.2** Material properties for the  $\text{SiO}_2$ , W, and Si layers in the thin film stack

Material	$E$ [GPa]	$\nu$	$\sigma_y$ [GPa]	$n$ [—]	$\alpha$ [%]	$\sigma_{RS}$ [GPa]
$\text{SiO}_2$	73	0.25	—	—	—	0.28
W	411	0.28	1.91	13.3	0.2	1.6
Si	170	0.28	—	—	—	—

Young's modulus  $E$ , Poisson's ration  $\nu$ , yield strength  $\sigma_y$ , hardening exponent  $n$ , and the yield offset  $\alpha$ . The constant value of the residual stresses  $\sigma_{RS}$  in the  $\text{SiO}_2$  and W layers

infinitely hard.  $\text{SiO}_2$  is considered to behave linear elastically and W is the material for which a stress–strain behavior following a Ramberg–Osgood material model is introduced [122]. The mechanical parameters used in the fracture simulations are given in Table 2.2, where it can be noted that the Young’s modulus values are within the range discussed in Sect. 2.3.3 and given in Appendix Table 2.5. However, the internal loading does not induce component failure, as the CDF never exceeds the critical  $J$ -integral  $J_{C, \text{SiO}_2}$  in the  $\text{SiO}_2$  layer.

The CDF is strongly increased when the crack is elongated into the W layer and towards the second IF. The anti-shielding effect from the yield strength inhomogeneity effect at the first IF is much more evident here, as the CDF from the EPRS calculation is significantly higher. While the crack is extended towards the second IF, the slope of the LERS/EPRS curve increases/decreases. From theory we know that  $J_{\text{tip}} \rightarrow \infty$  if the crack tip is situated directly at an IF with an anti-shielding effect. In the present case, the second IF has an anti-shielding effect from the Young’s modulus and a shielding effect from the yield strength inhomogeneity;  $J_{\text{tip}}$  increases faster towards the second IF when the elastic–plastic material properties are omitted. Most importantly, the CDF reaches and surpasses the  $J_{C, W}$  value, which would result in unstable crack propagation and critical failure of the entire structure.

For a clearer picture regarding the shielding/anti-shielding effect at the second IF, the system was externally loaded in addition to the internal loading. Displacement controlled loading was used in this test case, as it resembles the loading conditions from micro-cantilever beam fracture experiments [119]. The CDF close to the second IF is notably lower when calculated from the EPRS model, as shown in Fig. 2.21b. Interestingly, in a linear elastic calculation where the residual stresses are disregarded (LE in Fig. 2.21b) the CDF is significantly lower compared to the results from the simulations with internal loading. It is clear that the tensile residual stresses and the stress field in front of the crack tip from external loading add up to a higher value of the CDF. But especially in the W layer, the CDF calculated from the LE case does not even reach  $J_{C, W}$  and would therefore resist failure if the W layer would not suffer from such high tensile residual stresses (Table 2.2).

It seems that the high tensile residual stress state has the largest impact on the CDF in the material system. Even in the case without external loading, as shown in Fig. 2.21a, the resulting CDF is too high for the W layer to facilitate failure resistance.

We can conclude that it is crucial to consider the residual stress state as well as the proper material behavior in such thin film stacks. Although the flow behavior is not the deciding factor for critical failure in this particular system, in a different scenario it will, together with the residual stresses, definitely play an important role when it comes to the optimal design of material stacks.

## 2.6 Conclusions

This chapter offers an overview of the most important aspects for the modeling of semiconductor metal oxide gas sensor hotplates. After a historical overview, describing the need and development of the gas sensor, Section 2.1 describes the importance and the application of gas sensors in different markets. Subsequently, the importance of the Finite Element Method to model the mechanical stability of the hotplate, the temperature distribution over the active area, and the power consumption of the sensor is described.

Section 2.2 describes how specific geometries of the hotplate can maximize its performance by limiting the heat losses. Different concepts for the hotplate designs are analyzed, along with a list of most frequently used materials to realize the components of the sensor. Section 2.3 puts in evidence the material properties, which influence mostly the heat conduction and convection, and therefore strongly influence the electro-thermal performance and, consequently, play a significant role in the ability to perform accurate simulations of the device. A description of the main techniques used to characterize these properties concludes this section.

Section 2.4 describes our simulations of the hotplate during operation. The electro-thermal model matches very well the measured resistance variation and power dissipation of the hotplate, showing the validity of the assumptions made and the hypothesis of our FEM model. Deviations of the simulation from the characterized temperature profile are observed at high temperatures. A possible reason is the application of several approximations used in order to extract the temperature from the experimental resistance data.

The end of Section 2.4 and Section 2.5 deal with the mechanical behavior of the hotplate membrane. The limited knowledge for the values of the residual stress of the layers forming the membrane did not prevent the FEM model to predict a realistic membrane deformation, in agreement with the experimental observations. The tendency of the crack failure of the multilayer forming the membrane has been analyzed using the configurational force concept. This increases the general understanding of how the interfaces between silicon dioxide and tungsten could shield from crack propagation. The calculations also show that the high level of tensile stress in the tungsten layer has a strong influence on the crack driving force. This means that knowing the exact value of the residual stress in the layers forming the hotplate are of critical importance to understanding the device's mechanical reliability.

## Appendix: Thermo-Mechanical Properties of W, SiO<sub>2</sub>, and Si<sub>3</sub>N<sub>4</sub>

**Table 2.3** Thermal conductivities of selected materials

Composition	Property (W/m·K) at various temperatures (K)						
	300	400	500	600	800	1000	1200
W (bulk)	174	159	–	137	125	118	113
W (240 nm)	50–60	–	–	–	–	–	–
W (193 nm)	50	–	–	–	–	–	–
SiO <sub>2</sub> (bulk)	1.39	1.51	–	1.75	2.17	2.87	4
SiO <sub>2</sub> (1.74 μm)	0.68	0.57	0.48	–	–	–	–
SiO <sub>2</sub> (3.04 μm)	0.98	0.8	0.68	–	–	–	–
Si <sub>3</sub> N <sub>4</sub> (bulk)	16	13.9	–	11.3	9.88	8.76	8
Si <sub>3</sub> N <sub>4</sub> (0.6 μm)	12	12.7	–	–	–	–	–
Si <sub>3</sub> N <sub>4</sub> (1.4 μm)	8.1	8.5	–	–	–	–	–

Numerical values of the thermal conductivity of selected materials are taken from [123–128]

**Table 2.4** Thermal capacitance of selected materials

Composition	Property (J/kg·K) at various temperatures (K)						
	300	400	500	600	800	1000	1300
W (bulk)	–	140	139	141	144	–	145
W (bulk)	160	245	255	–	–	–	–
W (bulk)	132	–	–	–	–	–	–
SiO <sub>2</sub> (bulk)	725	–	–	–	–	–	–
SiO <sub>2</sub> (bulk)	1000	–	–	–	–	–	–
SiO <sub>2</sub> (glass)	–	–	~960	~1010	~1040	–	–
Si <sub>3</sub> N <sub>4</sub> (bulk)	700	–	–	–	–	–	–
Si <sub>3</sub> N <sub>4</sub> (1.5 μm)	500	720	~900	–	–	–	–
Si <sub>3</sub> N <sub>4</sub> (bulk)	800	–	–	–	–	–	–

Numerical values of the thermal capacitance of selected materials are taken from [126, 128–135]

**Table 2.5** Mechanical properties of selected materials

Composition	Young's modulus (GPa) at various temperatures (K)				Tensile strength (GPa)
	300	600	800	1100	Property at 300 K
W (bulk)	395	–	378	349	1.51
W (bulk)	391	$E = 391 - 1.3e^{-2}T - 1.4e^{-5}T^2$			0.88 (pure)
W (sheet)	397	–	–	–	1.39 (1.57 mm)
SiO <sub>2</sub> (bulk)	78	71	78	–	0.2
SiO <sub>2</sub> (1 μm)	60.1	–	–	–	0.6 in air
SiO <sub>2</sub> (bulk)	59	–	–	–	1.2 in vacuum
Si <sub>3</sub> N <sub>4</sub> (bulk)	300	280	280	270	0.345–0.483
Si <sub>3</sub> N <sub>4</sub> (bulk)	320	$E = 320.4 - 0.0151Te^{-445/T}$			2.4 (thin film)
Si <sub>3</sub> N <sub>4</sub> (800 nm)	280	–	–	–	0.39 (1 μm)

Numerical values of the Young's modulus and the tensile strength of selected materials are taken from [136–152]

**Acknowledgements** Financial support by the Austrian Federal Government (in particular from Bundesministerium für Verkehr, Innovation und Technologie and Bundesministerium für Wissenschaft, Forschung und Wirtschaft) represented by Österreichische Forschungsförderungsgesellschaft mbH and the Styrian and the Tyrolean Provincial Government, represented by Steirische Wirtschaftsförderungsgesellschaft mbH and Standortagentur Tirol, within the framework of the COMET Funding Programme is gratefully acknowledged.

## References

1. W.H. Brattain, J. Bardeen, Surface properties of germanium. *Bell Syst. Tech. J.* **32**(1), 1–41 (1953)
2. T. Seiyama et al., A new detector for gaseous components using semiconductive thin films. *Anal. Chem.* **34**(11), 1502–1503 (1962)
3. P.J. Shaver, Activated tungsten oxide gas detectors. *Appl. Phys. Lett.* **11**(8), 255–257 (1967)
4. N. Taguchi, Gas-detecting device. U.S Patent 3,631,436, 28 Dec 1971
5. K. Kalantar-Zadeh et al., Intestinal gas capsules: A proof-of-concept demonstration. *Gastroenterology* **150**(1), 37–39 (2016)
6. E. Abad et al., Flexible tag microlab development: Gas sensors integration in RFID flexible tags for food logistic. *Sensors Actuators B Chem.* **127**(1), 2–7 (2007)
7. M. Ortel et al., Spray pyrolysis of ZnO–TFTs utilizing a perfume atomizer. *Solid State Electron.* **86**, 22–26 (2013)
8. M. Prasad et al., Design and fabrication of Sidiaphragm, ZnO piezoelectric film-based MEMS acoustic sensor using SOI wafers. *IEEE Trans. Semicond. Manuf.* **26**(2), 233–241 (2013)
9. D.D. Lee et al., Environmental gas sensors. *IEEE Sensors J.* **1**(3), 214–224 (2001)
10. MarketsandMarkets, Gas Sensors Market worth 1,297.6 Million USD by 2023, 2018. [Online]. <https://www.marketsandmarkets.com/PressReleases/gas-sensor.asp>. Accessed Jul 2018
11. World Health Organization, 9 out of 10 people worldwide breathe polluted air, but more countries are taking action, 2018. [Online]. <http://www.who.int/news-room/detail/02-05-2018-9-out-of-10-people-worldwide-breathe-polluted-air-but-more-countries-are-taking-action>. Accessed Jul 2018

12. Hemming Fire, Looking to the future of gas sensing—a new galaxy of possibilities, Hemming Group Ltd, 08 April 2010. [Online]. [http://www.hemmingfire.com/news/fullstory.php/aid/844/Looking\\_to\\_the\\_future\\_of\\_gas\\_sensing\\_\\_96\\_a\\_new\\_galaxy\\_of\\_possibilities\\_.html](http://www.hemmingfire.com/news/fullstory.php/aid/844/Looking_to_the_future_of_gas_sensing__96_a_new_galaxy_of_possibilities_.html). Accessed May 2018
13. J. Riegel et al., Exhaust gas sensors for automotive emission control. *Solid State Ionics* **152**, 783–800 (2002)
14. G.F. Fine et al., Metal oxide semi-conductor gas sensors in environmental monitoring. *Sensors* **10**(6), 5469–5502 (2010)
15. E. Kanazawa et al., Metal oxide semiconductor N2O sensor for medical use. *Sensors Actuators B Chem.* **77**(1–2), 72–77 (2001)
16. T. Konduru et al., A customized metal oxide semiconductor-based gas sensor array for onion quality evaluation: System development and characterization. *Sensors* **15**(1), 1252–1273 (2015)
17. A. Lahlalia et al., Modeling and simulation of novel semiconducting metal oxide gas sensors for wearable devices. *IEEE Sensors J.* **18**(5), 1960–1970 (2018)
18. S.Z. Ali et al., Nanowire hydrogen gas sensor employing CMOS micro-hotplate, in *Proceedings of IEEE Sensors 2009 Conference*, (2009)
19. H.M. Low et al., Thermal induced stress on the membrane in integrated gas sensor with micro-heater, in *Proceedings of the 1998 IEEE Electron Devices Meeting, Hong Kong*, (1998)
20. D.-D. Lee et al., Low power micro gas sensor, in *Solid-State Sensors and Actuators and Eurosensors IX.. Transducers' 95, IEEE*, (1995)
21. I. Simon et al., Micromachined metal oxide gas sensors: Opportunities to improve sensor performance. *Sensors Actuators B Chem.* **73**(1), 1–26 (2001)
22. R. Phatthanakun et al., Fabrication and control of thin-film aluminum microheater and nickel temperature Sensor, in *Electrical Engineering/Electronics, Computer, Telecommunications and Information Technology (ECTI-CON), IEEE*, (2011)
23. K. Zhang et al., Fabrication, modeling and testing of a thin film Au/Ti microheater. *Int. J. Therm. Sci.* **46**(6), 580–588 (2007)
24. L. Xu et al., Development of a reliable micro-hotplate with low power consumption. *IEEE Sensors J.* **11**(4), 913–919 (2011)
25. P. Bhattacharyya et al., A low power MEMS gas sensor based on nanocrystalline ZnO thin films for sensing methane. *Microelectron. Reliab.* **48**(11), 1772–1779 (2008)
26. U. Dibbern, A substrate for thin-film gas sensors in microelectronic technology. *Sensors Actuators B Chem.* **2**(1), 63–70 (1990)
27. I. Haneef et al., Thermal characterization of SOI CMOS micro hot-plate gas sensors, in *Thermal Investigations of ICs and Systems (THERMINIC), IEEE*, (2010)
28. S.Z. Ali et al., Tungsten-based SOI microhotplates for smart gas sensors. *IEEE J. Microelectromech. Syst.* **17**(6), 1408–1417 (2008)
29. W. Yan et al., Nickel membrane temperature sensor in micro-flow measurement. *J. Alloys Compd.* **449**(1–2), 210–213 (2008)
30. D. Monika et al., Design and simulation of MEMS based microhotplate as gas sensor. *Int. J. Adv. Eng. Res. Technol.* **2**, 2487–2492 (2013)
31. L. Mele et al., A molybdenum MEMS microhotplate for high-temperature operation. *Sensors Actuators A Phys.* **188**, 173–180 (2012)
32. V. Balakrishnan et al., Steady-state analytical model of suspended p-type 3C–SiC bridges under consideration of Joule heating. *J. Micromech. Microeng.* **27**(7), 075008 (2017)
33. J.F. Creemer et al., Microhotplates with TiN heaters. *Sensors Actuators A Phys.* **148**(2), 416–421 (2008)
34. G. Benn, Design of a Silicon Carbide Micro-Hotplate Geometry for High Temperature Chemical Sensing, M.S. thesis (MIT, Cambridge, 2001)
35. J. Spannhake et al., High-temperature MEMS heater platforms: Long-term performance of metal and semiconductor heater materials. *Sensors* **6**(4), 405–419 (2006)
36. S.Z. Ali et al., A low-power, low-cost infra-red emitter in CMOS technology. *IEEE Sensors J.* **15**(12), 6775–6782 (2015)

37. A. Lahlalia et al., Electro-thermal simulation & characterization of a microheater for SMO gas sensors. *J. Microelectromech. Syst.* **27**(3), 529–537 (2018)
38. I. Elmi et al., Development of ultra-low-power consumption MOX sensors with ppb-level VOC detection capabilities for emerging applications. *Sensors Actuators B Chem.* **135**(1), 342–351 (2008)
39. J.C. Belmonte et al., High-temperature low-power performing micromachined suspended micro-hotplate for gas sensing applications. *Sensors Actuators B Chem.* **114**(2), 826–835 (2006)
40. J. Li et al., Dynamic characteristics of transient boiling on a square platinum microheater under millisecond pulsed heating. *Int. J. Heat Mass Transf.* **51**(1/2), 273–282 (2008)
41. S.M. Lee et al., Design and optimisation of a high-temperature silicon micro-hotplate for nanoporous palladium pellistors. *Microelectron. J.* **34**(2), 115–126 (2003)
42. F. Udrea et al., Design and simulations of SOI CMOS micro-hotplate gas sensors. *Sensors Actuators B Chem.* **78**(1–3), 180–190 (2001)
43. Y. Çengel et al., *Fundamentals of Thermal-Fluid Sciences* (McGraw-Hill, New York, 2001)
44. C. Dücsö et al., Porous silicon bulk micromachining for thermally isolated membrane formation. *Sensors Actuators A Phys.* **60**(1–3), 235–239 (1997)
45. A.I. Uddin et al., Low temperature acetylene gas sensor based on Ag nanoparticles-loaded ZnO-reduced graphene oxide hybrid. *Sensors Actuators B Chem.* **207**, 362–369 (2015)
46. R. Artzi-Gerlitz et al., Fabrication and gas sensing performance of parallel assemblies of metal oxide nanotubes supported by porous aluminum oxide membranes. *Sensors Actuators B Chem.* **136**(1), 257–264 (2009)
47. M. Aslam et al., Polyimide membrane for micro-heated gas sensor array. *Sensors Actuators B Chem.* **103**(1–2), 153–157 (2004)
48. T. Taliercio et al., Realization of porous silicon membranes for gas sensor applications. *Thin Solid Films* **255**(1–2), 310–312 (1995)
49. S. Astié et al., Design of a low power SnO<sub>2</sub> gas sensor integrated on silicon oxynitride membrane. *Sensors Actuators B Chem.* **67**(1–2), 84–88 (2000)
50. G. Wiche et al., Thermal analysis of silicon carbide based micro hotplates for metal oxide gas sensors. *Sensors Actuators A Phys.* **123**, 12–17 (2005)
51. T. Zhang et al., Electrochemically functionalized single-walled carbon nanotube gas sensor. *Electroanalysis* **18**(12), 1153–1158 (2006)
52. J. Li et al., A gas sensor array using carbon nanotubes and microfabrication technology. *Electrochem. Solid-State Lett.* **8**(11), H100–H102 (2005)
53. K.D. Mitzner et al., Development of a micromachined hazardous gas sensor array. *Sensors Actuators B Chem.* **93**(1–3), 92–99 (2003)
54. V. Guarnieri et al., Platinum metallization for MEMS application: Focus on coating adhesion for biomedical applications. *Biomatter* **4**(1), e28822 (2014)
55. Q. Zhou et al., Fast response integrated MEMS microheaters for ultra low power gas detection. *Sensors Actuators A* **223**, 67–75 (2015)
56. D.G. Cahill et al., Thermometry and thermal transport in micro/nanoscale solid-state devices and structures. *J. Heat Transf.* **124**(2), 223–241 (2002)
57. D.G. Cahill, Analysis of heat flow in layered structures for time-domain thermoreflectance. *Rev. Sci. Instrum.* **75**(12), 5119 (2004)
58. F. Claro, Theory of resonant modes in particulate matter. *Phys. Rev. B* **30**(9), 4989–4999 (1984)
59. S. Gomès et al., Scanning thermal microscopy: A review. *Phys. Status Solidi A* **212**(3), 477–494 (2015)
60. V. Szekely, Identification of RC networks by deconvolution: Chances and limits. *IEEE Trans. Circ. Syst. Fund. Theor. Appl.* **45**(3), 244–258 (1998)
61. L. Mitterhuber et al., Validation methodology to analyze the temperature-dependent heat path of a 4-chip LED module using a finite volume simulation. *Microelectron. Reliab.* **79**, 462–472 (2017)

62. A.J. Schmidt et al., Pulse accumulation, radial heat conduction, and anisotropic thermal conductivity in pump-probe transient thermoreflectance. *Rev. Sci. Instrum.* **79**, 114902(9) (2008)
63. P.B. Allen et al., Diffusons, locons and propagons: Character of atomic vibrations in amorphous Si. *Philos. Mag. B* **79**(11–12), 1715–1731 (1999)
64. M. Flik et al., Heat transfer regimes in microstructures. *J. Heat Transf.* **114**(3), 666–674 (1992)
65. G. Chen, Nonlocal and nonequilibrium heat conduction in the vicinity of nanoparticles. *J. Heat Transf.* **118**(3), 539–545 (1996)
66. J.Å. Schweitz, Mechanical characterization of thin films by micromechanical techniques. *MRS Bull.* **17**(7), 34–45 (1992)
67. V.M. Paviot et al., Measuring the mechanical properties of thin metal films by means of bulge testing of micromachined windows. *MRS Online Proc. Libr. Arch.* **356**, 579–584 (1994)
68. S. Mahabunphachai et al., Investigation of size effects on material behavior of thin sheet metals using hydraulic bulge testing at micro/meso-scales. *Int. J. Mach. Tools Manuf.* **48**(9), 1014–1029 (2008)
69. T.P. Weihs et al., Mechanical deflection of cantilever microbeams: A new technique for testing the mechanical properties of thin films. *J. Mater. Res.* **3**(5), 931–942 (1988)
70. X. Song et al., Residual stress measurement in thin films at sub-micron scale using focused ion beam milling and imaging. *Thin Solid Films* **520**(6), 2073–2076 (2012)
71. M. Krottenthaler et al., A simple method for residual stress measurements in thin films by means of focused ion beam milling and digital image correlation. *Surf. Coat. Technol.* **215**, 247–252 (2013)
72. N. Sabaté et al., FIB-based technique for stress characterization on thin films for reliability purposes. *Microelectron. Eng.* **84**, 1783–1787 (2007)
73. S. Massl et al., A direct method of determining complex depth profiles of residual stresses in thin films on a nanoscale. *Acta Mater.* **55**, 4835–4844 (2007)
74. G. Moser et al., Sample preparation by metallography and focused ion beam for nanomechanical testing. *Pract. Metallogr.* **49**(6), 343–355 (2012)
75. D. Kiener et al., Source truncation and exhaustion: Insights from quantitative in situ TEM tensile testing. *Nano Lett.* **11**(9), 3816–3820 (2011)
76. D. Kiener et al., Strength, hardening, and failure observed by in situ TEM tensile testing. *Adv. Eng. Mater.* **14**(11), 960–967 (2012)
77. M.F. Dorner et al., Stresses and deformation processes in thin films on substrates. *CRC Crit. Rev. Solid State Mater. Sci.* **14**(3), 225–267 (1988)
78. P. Chaudhari, Grain growth and stress relief in thin films. *J. Vac. Sci. Technol.* **9**(1), 520–522 (1972)
79. R.W. Hoffman, Stresses in thin films: The relevance of grain boundaries and impurities. *Thin Solid Films* **34**, 185–190 (1976)
80. E. Klokholm et al., Intrinsic stress in evaporated metal films. *J. Electrochem. Soc.* **115**(8), 823–826 (1968)
81. B.W. Sheldon et al., Intrinsic compressive stress in polycrystalline films with negligible grain boundary diffusion. *J. Appl. Phys.* **94**(2), 948–957 (2003)
82. E. Chason et al., Origin of compressive residual stress in polycrystalline thin films. *Phys. Rev. Lett.* **88**(15), 156103 (2002)
83. K. Cholevas, Misfit dislocation patterning in thin films. *Phys. Status Solidi B* **209**(10), 295–304 (1998)
84. L.B. Freund et al., *Thin Film Materials: Stress, Defect Formation and Surface Evolution* (Cambridge University Press, Cambridge, 2003)
85. P. Tsilingiris, Thermal conductivity of air under different humidity conditions. *Energy Convers. Manag.* **49**, 1098–1110 (2008)
86. A. Moridi et al., Residual stresses in thin film systems: Effects of lattice mismatch, thermal mismatch and interface dislocations. *Int. J. Solids Struct.* **50**(22–23), 3562–3569 (2013)

87. H. Köstenbauer et al., Annealing of intrinsic stresses in sputtered TiN films: The role of thickness-dependent gradients of point defect density. *Surf. Coat. Technol.* **201**, 4777–4780 (2007)
88. R. Machunze et al., Stress and strain in titanium nitride thin films. *Thin Solid Films* **517**, 5888–5893 (2009)
89. R. Treml et al., High resolution determination of local residual stress gradients in single- and multilayer thin film systems. *Acta Mater.* **103**, 616–623 (2016)
90. R. Hammer et al., High resolution residual stress gradient characterization in W/TiN-stack on Si(100): Correlating in-plane stress and grain size distributions in W sublayer. *Mater. Des.* **132**, 72–78 (2017)
91. R. Konetschnik et al., Micro-mechanical in situ measurements in thin film systems regarding the determination of residual stress, fracture properties and Interface toughness. *Microsc. Microanal.* **23**, 750–751 (2017)
92. J. Keckes et al., X-ray nanodiffraction reveals strain and microstructure evolution in nanocrystalline thin films. *Scr. Mater.* **67**, 748–751 (2012)
93. C. Genzel, X-ray residual stress analysis in thin films under grazing incidence—basic aspects and applications. *Mater. Sci. Technol.* **21**, 10–18 (2005)
94. J. Todt et al., X-ray nanodiffraction analysis of stress oscillations in a W thin film on through-silicon via. *J. Appl. Crystallogr.* **49**, 182–187 (2016)
95. M. Stefanelli et al., X-ray nanodiffraction reveals stress distribution across an indented multilayered CrN–Cr thin film. *Acta Mater.* **85**, 24–31 (2015)
96. R. Schöngrundner et al., Critical assessment of the determination of residual stress profiles in thin films by means of the ion beam layer removal method. *Thin Solid Films* **564**, 321–330 (2014)
97. M. Sebastiani et al., Depth-resolved residual stress analysis of thin coatings by a new FIB–DIC method. *Mater. Sci. Eng. A* **528**, 7901–7908 (2011)
98. T.L. Anderson, *Fracture Mechanics: Fundamentals and Applications* (CRC, Boca Raton, 2017)
99. M. Kuna, *Finite Elements in Fracture Mechanics: Theory—Numerics—Applications. Solid Mechanics and Its Applications* (Springer, Dordrecht, 2015)
100. O. Kolednik, *Fracture Mechanics, Wiley Encyclopedia of Composites* (Wiley, New York, 2011)
101. X.K. Zhu et al., Review of fracture toughness (G, K, J, CTOD, CTOA) testing and standardization. *Eng. Fract. Mech.* **85**, 1–46 (2012)
102. G. Irwin, Analysis of stresses and strains near the end of a crack traversing a plate. *J. Appl. Mech.* **24**(3), 361–364 (1957)
103. A.A. Griffith, The phenomena of rupture and flow in solids. *Philos. Trans. R. Soc. A Math. Phys. Eng. Sci.* **221**(582–593), 163–198 (1921)
104. J.R. Rice, A path independent integral and the approximate analysis of strain concentration by notches and cracks. *J. Appl. Mech.* **35**(2), 379–386 (1968)
105. N.K. Simha et al., J-integral and crack driving force in elastic-plastic materials. *J. Mech. Phys. Solids* **56**(9), 2876–2895 (2008)
106. O. Kolednik et al., A new view on J-integrals inelastic–plastic materials. *Int. J. Fract.* **187**(1), 77–107 (2014)
107. R.O. Ritchie, Mechanisms of fatigue crack propagation in metals, ceramics and composites: Role of crack tip shielding. *Mater. Sci. Eng.* **103**(1), 15–28 (1988)
108. N.K. Simha et al., Inhomogeneity effects on the crack driving force in elastic and elastic-plastic materials. *J. Mech. Phys. Solids* **51**(1), 209–240 (2003)
109. R.O. Ritchie et al., Fatigue crack propagation in ARALL<sup>®</sup> LAMINATES: Measurement of the effect of crack-tip shielding from crack bridging. *Eng. Fract. Mech.* **32**(3), 361–377 (1989)
110. O. Kolednik et al., Improvement of fatigue life by compliant and soft interlayers. *Scr. Mater.* **113**, 1–5 (2016)
111. Y. Sugimura et al., Fracture normal to a biomaterial interface: Effects of plasticity on crack-tip shielding and amplification. *Acta Metall. Mater.* **43**(3), 1157–1169 (1995)

112. J. Predan et al., On the local variation of the crack driving force in a double mismatched weld. *Eng. Fract. Mech.* **74**(11), 1739–1757 (2007)
113. O. Kolednik et al., Modeling fatigue crack growth in a bimaterial specimen with the configurational forces concept. *Mater. Sci. Eng. A* **519**(1–2), 172–183 (2009)
114. N.K. Simha et al., Material force models for cracks—influences of eigenstrains, thermal strains & residual stresses, in *11th International Conference on Fracture*, (2005)
115. J.D. Eshelby, *Energy Relations and the Energy-Momentum Tensor in Continuum Mechanics BT* (Springer, Berlin, 1999)
116. M.E. Gurtin, *Configurational Forces as Basic Concepts of Continuum Physics* (Springer, New York, 2000)
117. G.A. Maugin, *Configurational Forces: Thermodynamics, Physics, Mathematics, and Numerics* (CRC, Boca Raton, 2010)
118. N.K. Simha et al., Crack tip shielding or anti-shielding due to smooth and discontinuous material inhomogeneities. *Int. J. Fract.* **135**(1), 73–93 (2005)
119. R. Trembl et al., Miniaturized fracture experiments to determine the toughness of individual films in a multilayer system. *Extreme Mech. Lett.* **8**, 235–244 (2016)
120. B. Merle et al., Fracture toughness of silicon nitride thin films of different thicknesses as measured by bulge tests. *Acta Mater.* **59**, 1772–1779 (2011)
121. E. Harry et al., Mechanical properties of W and W(C) thin films: Young’s modulus, fracture toughness and adhesion. *Thin Solid Films* **332**, 195–201 (1998)
122. D. Kozic et al., Extracting flow curves from nano-sized metal layers in thin film systems. *Scr. Mater.* **130**, 143–147 (2017)
123. G. Klemes, *Thermal Conductivity: Metallic Elements and Alloys* (Plenum, New York, 1970)
124. J. Hostetler et al., Thin-film thermal conductivity and thickness measurements using picosecond ultrasonics. *Microsc. Thermophys. Eng.* **1**(3), 237–244 (1997)
125. L. Xiang, Thermal conductivity modeling of copper and tungsten damascene structures. *J. Appl. Phys.* **105**(9), 094301 (2009)
126. T.L. Bergman et al., *Fundamentals of Heat and Mass Transfer* (Wiley, New York, 2011)
127. H.A. Schafft et al., Thermal conductivity measurements of thin-film silicon dioxide in microelectronic test structures, in *Microelectronic Test Structures (ICMETS), IEEE*, (1989)
128. X. Zhang et al., Thermal conductivity and diffusivity of free-standing silicon nitride thin films. *Rev. Sci. Instrum.* **66**(2), 1115–1120 (1995)
129. Texas Instruments, Thermal conductivity and thermal diffusivity, Report (2014)
130. P.I. Dorogokupets et al., Optimization of experimental data on the heat capacity, volume, and bulk moduli of minerals. *Petrology* **7**(6), 574–591 (1999)
131. S. Andersson, Thermal conductivity and heat capacity of amorphous SiO<sub>2</sub>: pressure and volume dependence. *J. Phys. Condens. Matter* **4**(29), 6209 (1992)
132. A.S. Grove, *Physics and Technology of Semiconductor Devices* (Wiley, New York, 1967)
133. T. Ohmura et al., Specific heat measurement of high temperature thermal insulations by drop calorimeter method. *Int. J. Thermophys.* **24**(2), 559–575 (2003)
134. C.H. Mastrangelo et al., Thermophysical properties of low-residual stress, silicon-rich, LPCVD silicon nitride films. *Sensors Actuators A Phys.* **23**(1–3), 856–860 (1990)
135. A. Jain et al., Measurement of the thermal conductivity and heat capacity of freestanding shape memory thin films using the  $3\omega$  method. *J. Heat Transf.* **130**(10), 102402 (2008)
136. J. Harrigill et al., Method for Measuring Static Young’s Modulus of Tungsten to 1900 K (1972)
137. J.W. Davis et al., ITER material properties handbook. *J. Nucl. Mater.* **233**, 1593–1596 (1996)
138. G.P. Škoro et al., Dynamic Young’s moduli of tungsten and tantalum at high temperature and stress. *J. Nucl. Mater.* **409**(1), 40–46 (2011)
139. D. Makwana et al., Review of miniature specimen tensile test method of tungsten at elevated temperature. *Int. J. Eng. Dev. Res.* **4**(4), 132–139 (2016)
140. S. Krimpalis et al., Comparative study of the mechanical properties of different tungsten materials for fusion applications. *Phys. Scripta* **2017**(T170), 014068 (2017)

141. F.F. Schmidt et al., *The Engineering Properties of Tungsten and Tungsten Alloys, No. DMIC191* (Battelle Memorial Institute, Defense Metals Information Center, Columbus, 1963)
142. T. Shinoda et al., Young's modulus of RF-sputtered amorphous thin films in the SiO<sub>2</sub>-Y<sub>2</sub>O<sub>3</sub> system at high temperature. *Thin Solid Films* **293**(1–2), 144–148 (1997)
143. O. Morozov et al., Mechanical strength study of SiO<sub>2</sub> isolation blocks merged in silicon substrate. *J. Micromech. Microeng.* **25**(1), 015014 (2014)
144. W.N. Sharpe et al., Strain measurements of silicon dioxide microspecimens by digital imaging processing. *Exp. Mech.* **47**(5), 649–658 (2007)
145. T. Tsuchiya et al., Tensile testing of insulating thin films; humidity effect on tensile strength of SiO<sub>2</sub> films. *Sensors Actuators A Phys.* **82**(1–3), 286–290 (2000)
146. J.-H. Zhao et al., Measurement of elastic modulus, Poisson ratio, and coefficient of thermal expansion of on-wafer submicron films. *J. Appl. Phys.* **85**(9), 6421–6424 (1999)
147. E. Sánchez-González et al., Effect of temperature on the pre-creep mechanical properties of silicon nitride. *J. Eur. Ceram. Soc.* **29**(12), 2635–2641 (2009)
148. aZo Materials, Sintered Silicon Nitride (Si<sub>3</sub>N<sub>4</sub>), [Online]. <https://www.azom.com/properties.aspx?ArticleID=260>
149. R.J. Bruls et al., The temperature dependence of the Young's modulus of MgSiN<sub>2</sub>, AlN and Si<sub>3</sub>N<sub>4</sub>. *J. Eur. Ceram. Soc.* **21**(3), 263–268 (2001)
150. A.E. Kaloyeros et al., Silicon nitride and silicon nitride-rich thin film technologies: Trends in deposition techniques and related applications. *ECS J. Solid State Sci. Technol.* **6**(10), 691–714 (2017)
151. A. Khan et al., Young's modulus of silicon nitride used in scanning force microscope cantilevers. *J. Appl. Phys.* **95**(4), 1667–1672 (2004)
152. G.F. Cardinale et al., Fracture strength and biaxial modulus measurement of plasma silicon nitride films. *Thin Solid Films* **207**(1–2), 126–130 (1992)